Influence of microstructure on surface characteristics in cold-deformed stainless steel tubes
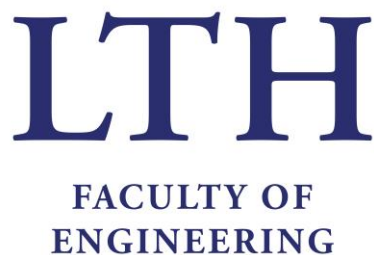
Fredrik Ottenklev
May 2019

Supervisor: Professor Dmytro Orlov, Lund University

Cosupervisor: Dr. Martin Adell, Tetra Pak Processing Systems AB

Examiner: Professor Srinivasan Iyengar, Lund University

Faculty of Engineering, Lund university
Lund

Abstract

Cold deformation of metals is known to induce roughness on their free surface. In some of the processing equipment of Tetra Pak processing systems, tubes of austenitic stainless steel 316L are used. During the production of this processing equipment, such tubes are occasionally cold-deformed. In this work, surface and microstructure characterization of alloying type 316L austenitic stainless steel has been performed to understand how the cold deformation during production process affects the surface structure of the material. Prime focus of the study has been the relationship between tensile strain and surface roughness on polished and unpolished 316L samples. It is shown that in *polished* steel sheets, surface roughness increases to a maximum with the increase of engineering strain level up to 15 %. Thereafter roughness decreases slightly and settles at a level where the roughness is no longer affected by the strain. The roughness was found to be localized primarily in the vicinity of grain boundaries. Further analysis reveals that the roughness-strain correlation can be explained by grain rotation and subdivision. *Unpolished* sheets demonstrated approximately linear relationship between tensile strain and surface roughening. They had a passivation layer on the surface, as confirmed by SEM and EDS measurements. The passivation layer has a thickness of 1 μm and demonstrates scale-like structure with the morphology of underlying austenitic microstructure in the substrate. When strained, it appeared to inherit two roughness components. First one is a shortwave component originating at the boundaries of the scale, which is believed to be produced by the rotation of the underlying grains. The second one is a longwave component, which is generated by the cracking of scale due to the lack of ductility. The latter prevents the oxide layer to deform plastically and conformally with the macroscopic specimen strain. The slope of the roughness – true strain relationship was found to be orientation-dependent. The magnitude of the slope correlated to respective grain dimension. A model for biaxially strained steel tubes was also developed, which showed to be accurate within the dimension boundaries of interest. Techniques and instrumentation used in the thesis were tensile testing, 3D-focus varying optical microscopy, SEM, EBSD, EDS.

Keywords: Cold deformation, surface roughness, strain, microstructure, austenitic stainless steel, grain rotation

Sammanfattning

Kalldeformation av metaller är allmänt erkänt att inducera ojämnheter på deras fria yta. I processutrustning tillverkad hos Tetra Pak processing systems används stålrör av austenitiskt rostfritt stål, 316L, och är under delar av produktionen kalldeformerade. I detta arbete har yt- och mikrostrukturskaratärisering av 316L rostfritt stål utförts för att förstå hur kalldeformation under produktionsprocessen påverkar ytstrukturen. Fokus i denna studie har varit förhållandet mellan töjning och ytojämnhet av polerade och opolerade 316L prover. Det har visats att för polerad stålplåt så ökar ytojämnheten med töjning till att uppnå ett maximum vid 15 % töjning. Detta följs av en svag minskning i ytojämnhet tills en nivå nås där ytojämnheten inte längre ändras med töjning. Ytojämnheten har visat sig vara lokaliserad främst vid korngränser och analys indikerar att beteendet mellan ytojämnhet och töjning förklaras av kornrotation och översvägning av kornen. Opolerat stål uppvisade ett förhållande melln töjning och ytojämnhet som kunde approximeras som linjärt. Det innehade ett passiveringslager på ytan, bekräftat från SEM och EDS mätningar. Passiveringslagret var 1 μm tjockt och bestod av fjälllika strukturer med en morfologi likt den underliggande austenitiska kornstrukturen. Efter töjning framträdde vad som tolkades som två ytojämnhetskomponenter. Den ena, en kortvågig komponent lokaliserad vid gränserna mellan fjällen som tros härstamma från underliggande kornrotation. Den andra, en långvågig komponent som tros härstamma från en avsaknad av duktilitet vilket hindrar oxidlagret från att deformeras följsamt med den makroskopiska deformationen. Lutningskoefficienten för den linjära approximationen visade sig vara beroende av riktningen i vilken man mätte, där riktningen med störst lutningskoefficient också var den med störst avstånd mellan korngränserna. En modell för stålrör utsatta för biaxiell kallderformation via en inbuktningsprocess har utvecklats likväl, vilken var relativt pålitlig inom vissa geometriska dimensioner för inbuktningen. Tekniker och instrument använda i detta examensarbete är dragprovsmaskin, 3D fokusvarierande optisk mikroskopi, SEM, EBSD, EDS.

Nyckelord –Kalldeformation, ytjämnhet, töjning, mikrostruktur, austenitiskt rostfrit stål, kornrotation

Acknowledgements

Contents

Nomenclature

1D	One-dimensional
2D	Two-dimensional
3D	Three-dimensional
BCC	Body centered cubic
BSE	Backscattered electron
EBSD	Electron backscatter diffraction
EDS	Energy dispersive X-ray spectroscopy
EM	Electron microscopy
FCC	Face centered cubic
FEM	Finite element method
FFT	Fast Fourier transform
FV	Focus varying
HCP	Hexagonal close packed
ND	Normal direction
SEM	Scanning electron microscopy
Ra	Arithmetical mean average line roughness
RD	Roll direction
RMS	Root-mean-square
Rq	Root mean square line roughness
Sa	Arithmetical mean average surface roughness
SD	Standard deviation
SE	Secondary electron
Sq	Root mean square surface roughness
TD	Transverse direction
UTS	Ultimate tensile strength
YS	Yield strength

List of figures

1 Introduction

Tetra Pak® is a Swedish company based in Lund. It was established in 1951 by Ruben Rausing. The organization is divided into three businesses that are Tetra Pak processing, Tetra Pak packaging and Tetra Pak services. This thesis has been conducted at Tetra Pak® Processing Systems in a project of characterizing the behavior of the inner surface of 316L stainless steel tubes used in processing equipment.

Processing equipment produced at Tetra Pak are used to process liquid food products. The interface between the food flowing through the system and the processing equipment is the inner surface of the tubes. Therefore, it is important to acquire a good knowledge of the surface- and microstructure of the material in use to optimize the production process.

During the manufacturing process of processing equipment at Tetra Pak®, steel tubes are cold-deformed. Cold deformation is known to alter the surface structure of metals. It is of interest to investigate in detail the effect of cold deformation on the surface and the microstructure of 316L stainless steel in order to optimize the production process. The objective of this master's thesis is to characterize the microstructure and surface roughness of 316L stainless steel to determine what effect cold plastic deformation has on the surface of the material. To do this experimental work, primarily consisting of surface roughness measurements, tensile tests and electron microscopy of 316L stainless steel sheets have been conducted. A deeper understanding of the material *per se* has also been of interest during the project, which has been analyzed by electron backscatter diffraction. Equipment and techniques used in this thesis were 3D focus-varying optical microscopy, tensile testing, electron microscopy (EM), energy dispersive X-ray spectroscopy (EDS) and electron backscatter diffraction (EBSD). The results of this project are expected to be complemented with another master's thesis project carried out at FS dynamics. The latter aims to create a mechanical model of cold deformation on steel tubes using the finite element method (FEM). The ultimate goal of these two projects is to elaborate tools capable of predicting surface roughness evolution in cold deformation.

The goals of this master's thesis are to:

- Determine the mechanism of strain-induced surface roughness evolution in 316L stainless steel;
- Establish a correlation between the evolution of surface roughness and microstructure in 316L stainless steel during cold deformation;
- Develop a model describing the relationship between strain and surface roughness evolution.

2 Literature survey

In order to understand the correlation between cold deformation process and surface roughness in steel tubes used in processing equipment, it is very important to understand (i) basic deformation mechanisms of metals, (ii) definition of surface roughness, and (iii) how these two properties are interconnected. A literature survey was therefore carried out to assess already established knowledge of the subject. Main findings from this survey are presented in the following section.

2.1 Cold deformation

The most typical deformation mechanism in metals is dislocation slip. This is the case for alloying type 316L stainless steel while twinning is another prominent deformation mechanism in this material. Dislocation slip is a process when one part of a crystal 'slide' over the other by dislocation movement in a certain crystallographic plane[1]. 316L steel is 'austenitic', which means face centered cubic (FCC) crystal structure is stable at ambient temperature conditions. The weakest interplanar bonds within such a crystal is between the close packed planes. These are defined as the planes with the most atoms per unit area and are the (111) planes in FCC metals. These planes must have the largest interplanar distance and thus also to have the weakest interplanar bonding forces. The most prominent slip directions thus lie within these planes. The primary slip plane and slip directions (making up the slip system) of an FCC metal is illustrated in Figure 2.1, based on [2].
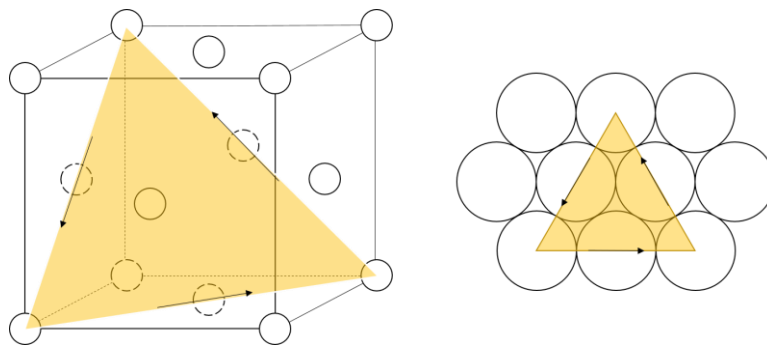
Figure 2.1: Schematic drawing of a unit cell in FCC lattice structure with a close packed (111) plane indicated together with arrows pointing towards possible slip directions. Adapted from [2].

Figure 2.1 illustrates how the close packed planes of {111} type is oriented within the atomic structure and indicates the slip directions of <110> type with black arrows. From the two schematics in this figure, it can be understood that if slip occurs in one of the primary directions (one plane slips over a parallel underlying plane), respective atoms move a whole interatomic distance, and relative atomic positions of the two planes remain the same with all the atoms shifted for one 'atomic step'. However, there are two different ways of having two overlapping close-packed crystal planes, as is illustrated in Figure 2.2.
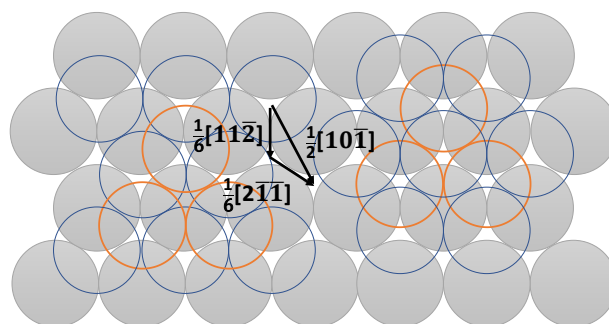
Figure 2.2: Schematic drawing illustrating atomic positions of FCC planes, with primary slip vector [110] and slip step vectors <112> indicated by arrows

2

As seen in Figure 2.2 above, from a given crystal plane (gray), it is possible to position two overlying planes (blue and orange) in two different ways. It is possible during a deformation process that instead of having a proper slip where an atom plane remains in the original relation to the underlying plane (shifted in [110] direction), they instead shift to a new relative position (shifted in [112] direction). This process results in 'twinning', which can be either 'mechanical', if it is an effect of a deformation process, or 'annealing', if it is the result of 'faulty' stacking in recrystallization when new grains are formed.

During slip processes of polycrystalline material, rotation of grains is induced. Grain rotation occurs when a slip system is exposed to shear stress in a grain, which is geometrically restricted to free-form. The resolved shear stress of a slip system exposed to a tensile force is given by the Schmidt factor, which is a function of the angles between tensile axis, slip plane and slip direction. Equations (1) and (2) show the relationship between resolved shear stress and the Schmidt factor, and allow to calculate the Schmidt factor, respectively:

$$\tau = m\sigma \tag{1}$$

$$m = cos\phi \ sin\lambda \tag{2}$$

When sufficiently high load is applied to a crystal, the slip system having the highest Schmidt factor becomes activated. Due to geometrical restrictions on a grain located within many others, larger slip distances within this plane is limited. Therefore, the grain starts rotating away from the orientation of maximum resolved shear stress instead. After a certain amount of rotation, the grain becomes oriented such that another slip system develops a similar Schmidt factor and becomes activated. However, the primary rotation continues somewhat before the activation of the secondary slip system, which is known as overshooting. After the activation of a secondary slip system, the grain rotates back towards the orientation where the Schmidt factors of the two slip systems are equal. Finally, a steady state is achieved [1].

2.2   Surface roughness

Surface roughness refers to the local out-of-plane deviations of a surface. To separate between roughness, which is local shortwave deviation and waviness, which is longwave components of a surface, profile filters are often used. The coordinate system in which surface parameters are to be determined is defined in ISO standard (SS-EN_ISO_4287) as an orthogonal rectangular system where the x- and y-axes are parallel to the material planes, and the z-axis is directed out of the plane formed by the x- and y-axes. Roughness can be described by various parameters. The relevant ones to be discussed in this thesis report are Sa, Ra, Sq and Rq. Sa and Ra will be in focus in the experimental part of the thesis, while the others is mostly discussed within literature survey. Ra is the arithmetical line average of the surface and Rq is the root mean square (RMS). They are defined according to equation (3) and (4) respectively.

$$Ra = \frac{1}{l}\int_l |Z(x)|dx \tag{3}$$

$$Rq = \sqrt{\frac{1}{l}\int_l Z^2(x)dx} \tag{4}$$

The zero value of z is the average spatial height of the surface. Ra is thus the sum of the area elements enclosed by the zero-value axis and the roughness profile, averaged over the entire measured length,

l. Rq is similarly averaged over the measured line but is instead integrated over the squared z-values [3].

Sa and Sq are similar but two-dimensional (2D) parameters. Instead of measuring over a line and integrating over one-dimensional (1D) space, one measures over a surface and integrates over its area. Sa is thus obtained as the sum of volume elements enclosed by the real surface and a reference plane, averaged over the area. Sa and Sq are extensions of Ra and Rq, respectively. Arithmetical average and RMS differ in that for Rq, large deviations are amplified, while they are averaged in Ra.

Both arithmetic average and root-mean-square, disregarding if it is surface- or line, have the disadvantage of representing a large amount of information in just a single value [4]. Figure 2.3 and Figure 2.4 below are good illustrations of how surfaces with quite different appearances can give rise to the same, or similar Ra and Rq-values.

Surface Profile	R_a
	0.2
	0.2
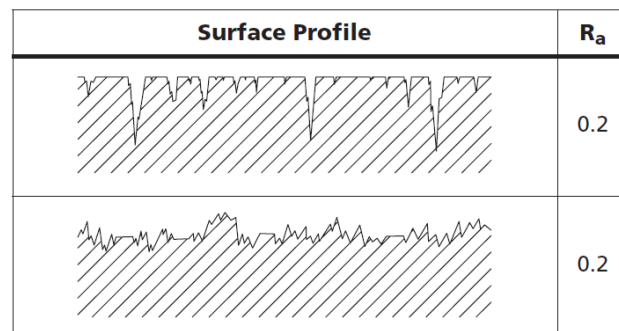
Figure 2.3: Two different surface cross-sections having the same Ra-value. Reproduced from [4]

Rq= 0.142 μm ± 0.023 μm   Rq= 0.144 μm ± 0.007 μm
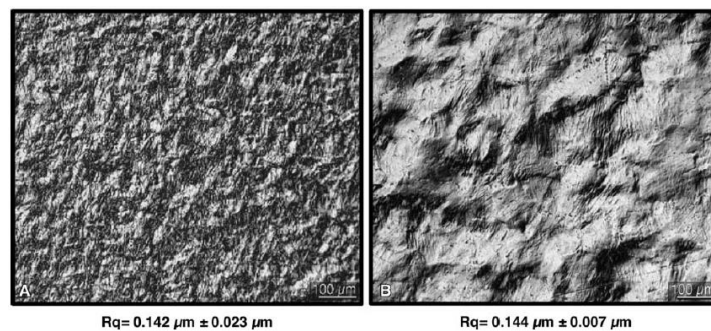
Figure 2.4: Two different surfaces both having the same Rq-value. Reproduced from [5]

Since surface parameters such as Ra and Rq are single-value parameters that represent a large amount of data, they are not optimal. However, they are well suited for the present study and are sufficiently descriptive to give an approximate representation of surface roughness. A parameter to be used in a particular case depends on specific circumstances. Since they are sensitive to different surface characteristics, it can be useful to work with both the parameters for complementarity.

2.2.1   Strain-induced surface roughness

When exposing a material to a stress above the yield point, plastic deformation takes place. This affects the surface structure of a material by increasing the roughness of a free surface [5-8]. Strain-induced surface roughening has been shown to derive from several mechanisms such as grain rotation (also known as grain boundary-localized roughness), twinning and formation of dislocation steps, listed in the order of surface roughness magnitude [5, 9-11].

In some studies, it has been found that there is a linear relationship between true plastic strain and surface roughness [6, 12]. True strain is the change in length with respect to the instant length. It is

calculated as the integral sum of infinitesimal elongations and is related to engineering strain according to equation (5).

$$e = \ln(1 + \varepsilon)$$ (5)

where e is true strain, and ε is engineering strain.

However, the linear relationship between surface roughness and true strain is questioned by Stoudt et al. [7]. They claim this to be an incorrect assumption resulting from the incorrect sampling of data. In another study by Stoudt and co-workers [13] performed on an aluminum alloy, it was shown that (i) the relationship is not necessarily linear, and (ii) the relationship depends on the grain size. For small grain sizes (about 50 μm) the relationship between surface roughness (Sq) and true plastic strain appeared linear. However, for larger grain sizes (120-160 μm) the relationship appeared positively quadratic. The conclusions that they drew on how the surface roughness relates to strain from the study was thus not unambiguous, but rather depends on the microstructure of the material. This conclusion that the relationship is not strictly linear can also be derived when comparing different papers reporting linear relationship. In particular, it was noted that among those who found linear relationship not everyone used the same parameter for surface roughness. Both Ra and Sq were investigated and were shown to be linearly correlated to e. However, since the relationship between RMS and arithmetical average is not linear, this indicates that the linear relationship cannot hold for at least one of these parameters. Even though the relationship is not strictly applied, it is still of interest since it might be a reliable approximation to use in a model.

2.2.2 Effect of microstructure

K. Osakada and M. Oyane derived a relationship between roughness rate and grain size as equation (6) below [6].

$$\alpha = kd$$ (6)

Where α is the roughness rate expressed as the center line average (Ra, Sa) over true plastic strain, k is a material constant and d is the grain size diameter. As can be seen, this equation is based on a linear relationship between strain and surface roughness.

The slip systems are dependent on the crystal structure of a material. Strain-induced surface roughness has been shown to be affected by slip and slip systems, and thereby also the crystal structure. For hexagonal close packed (HCP) material, the primary slip system is {0001} <11-20>, for face centered cubic it is {111} <110> and for body centered cubic (BCC) the slip planes are (110), {112} and {123} with the slip direction <111>. The total amount of slip systems for the different crystal structures are 3 (HCP), 12 (FCC) and 48 (BCC). In the study by Osakada and Oyane, they concluded that the amount of slip systems affects the roughness rate upon plastic deformation. The constant, k, from equation (6) was experimentally determined for different lattice structures to be roughly 1 for HCP metals, 0.5 for FCC metals and 0.2-0.25 for BCC metals. This shows that the tendency for roughening is higher in materials having less slip systems available. This is believed to be the case since grains with a higher amount of slip systems are capable to accommodate macroscopic deformation better [6].

Since 316L has FCC structure, the amount of slip systems is 12. However, austenite is only stable in a certain temperature region. During cooling, austenite can undergo a phase transformation to martensite. The temperature when this transformation occurs, M_s, for 316-type steels is far below room temperature. However, when exposed to severe strain the transformation can occur at higher temperatures [14]. Martensite is characterized by its residual stresses. The transformation from austenite to martensite is a diffusionless process and is entirely due to shear. This gives rise to a needle

like structure easily distinguishable from austenite [1]. Martensite exists in two phases, ε- and α'-martensite. α'-martensite is a ferromagnetic BCC phase and ε-martensite is a paramagnetic HCP phase. During deformation of austenite the majority transforms into α'-martensite by a quick process of γ→ε→α'. This was studied by H. F. G. Abreu et al. where they used x-ray diffraction and electron backscatter diffraction (EBSD) to analyze the amount of martensite formed during cold-rolling of 304 LN and 316L austenitic stainless steel [15]. How energetically favorable it is for martensite to form is highly dependent on the alloying composition of the material. Angel et al. suggest equation (7) below, as an approximate temperature at which 50 % of the austenite form into martensite at 30 % elongation.

$$M_d(°C) = 413 - 13.7(\%Cr) - 9.5(\%Ni) - 8.1(\%Mn) - 18.5(\%Mo) \qquad (7)$$
$$- 9.2(\%Si) - 462(\%[C + N])$$

Due to the needle like appearance of martensite one might expect a higher surface roughness of martensite compared to austenite, but it should also be considered that α'-martensite is a BCC phase and thus has prerequisites for a more uniform deformation with respect to the macro deformation and thus obtain a lower roughening rate than austenite. A hypothesis is then that if there are parts of the samples consisting of martensite these might have a higher initial surface roughness, but once deformed the roughening rate is lower possibly resulting in a low surface roughness. The production processes of interest in this study from the martensite formation perspective are sheet forming, welding with heat treatment and final cold deformation. If the as-supplied sheet metal was not fully annealed, the rolling-type microstructure and texture is the dominating deformation process during the formation of steel tubes and potentially form martensite. In this case, the welding of the tubes and heat treatment that follows may decrease the concentration of martensite. During the following cold deformation of tubes, the formation of martensite becomes possible again.

2.3 Surface structure of stainless steel

The corrosion resistance of 316L as well as other stainless steels is mainly due to a passive film generated on the surface when chromium reacts with oxygen to form chromium oxide. This is an admirable property for use in the food processing industry since many food products are acidic. For instance, in an article by Sanusi Kazeem Oladele and Hussein Kehinde Okoro, the corrosion effects of orange juice and other fruit juices was tested on a type of mild steel which clearly showed that the juices and in particular orange juice had a great corroding effect on the steel [16]. Since material investigated in this thesis project is used in equipment that is in some cases heated, the corrosion protection is extremely important since acidic corrosion on steel and iron relates exponentially to the temperature according to the Arrhenius equation [17, 18].

Although necessary in service, the passivation layer complicates microstructure characterization of underlying substrate steel by blocking the penetration of electrons and photons in microscopy. To enable the characterization of austenitic microstructure in the substrate steel, it is necessary to grind, polish and occasionally etch the samples.

2.4 3D measurements

Many techniques are available to measure surface roughness. These can be divided into two categories: the contact stylus and the non-contact techniques. In the contact stylus techniques, a needle, or stylus, is swept across a specimen to measure the height variations of the surface. These measurements do have disadvantages, such as direct contact with the sample. They are also limited in resolution by the size of stylus tip and how well the shape of the tip is defined. Non-contact

instruments are often based on some sort of light-sample interaction, but there is also electron microscopy and atomic force microscopy (if one considers this as a non-contact method) [19].

The technique that was used for surface roughness measurements in this thesis is non-contact focus varying (FV) optical microscopy. This technique operates by vertically scanning the focus from over- to under focus. With a small depth of field only certain parts of the topography are in focus at each frame. While scanning, software detects parts of the sample in focus at each scan height, merges them and maps out the topography of the sample. To obtain a large field of view, it is possible to scan the system also in x- and y-directions to stitch images together. Such a method is available in Alicona IF portable microscope that was used for surface roughness measurements in this thesis project. For large area measurements stitching is to be performed by raster scanning.

2.5   Microstructure analysis

Microstructures can be analyzed by various techniques. In modern laboratories, diffraction and imaging in electron microscopes are used routinely. In this thesis project, EBSD and scanning electron microscopy (SEM) was utilized. EBSD is a mature technique to analyze crystal orientations, grain boundary density and grain size distribution. EBSD is most often incorporated into a scanning electron microscope where an electron beam scans across a sample surface tilted for approximately 70° to the beam. A detector (often a fluorescent phosphor screen combined with a CCD-detector) is positioned in the scattering path of the electrons. It collects a diffraction pattern of distinct lines known as Kikuchi lines. The Kikuchi lines are formed by multiple scattering in the crystal planes and are related to the lattice structure and the crystal orientation of the specimen. By scanning electron beam over the specimen surface, information on local microstructure is obtained. In the end, individual areas can be combined to give a detailed structure of the entire sample surface [20].

Crystal orientation is often presented using stereographic projections. As mentioned above, the material to be investigated is a polycrystalline FCC metal. Hence, there are multiple crystallites (grains) in the material. They possess certain orientations. When a surface is prepared for diffraction measurements, the material is cut, so that certain crystallographic plane becomes exposed to the surface in each grain. Crystal plane oriented parallel to the cut surface would not be the same for all of the grains. Yet, in processes such as cold rolling and annealing grains tend to orient themselves in a certain crystal orientation related to the rolling direction. This makes some crystal planes more frequent on the surface thus revealing the material anisotropy [21, 22]. Stereographic projections are often used as an illustrative tool representing crystal planes parallel to a measured surface. In Figure 2.5, based on [23] and [1], below schematic illustrations of how (001) stereographic projection is constructed is seen.
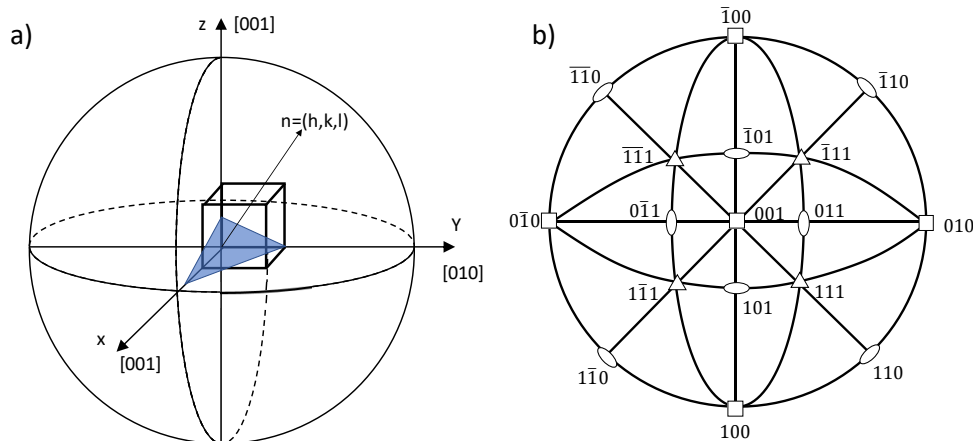
Figure 2.5: a) schematic drawing of how a stereographic projection is produced. Adapted from [23]. b) 001 stereographic projection. based on [1]

In the Figure 2.5a, a sphere with a coordinate system based on a cube is shown with the normal of (001) plane directed towards the upper pole used as the reference for projecting other planes. In the figure, plane (211) is highlighted in blue and the normal to this plane is projected to the surface of the sphere. This can be done for all necessary planes and can therefore be used to show crystallographic planes on a surface. Usually, a 2D projection of the sphere on equatorial section is created by looking at it from above. Such a projection is seen in Figure 2.5b, showing pole figures of certain crystallographic orientations. The frequency of particular crystal orientations is represented by an intensity scale, e.g. a thermal map, where red area indicates that many grains have that particular plane oriented parallel to the sample surface.

3 Material and Experimental Methods

This section describes the material studied along with how experiments and measurements were carried out. Samples in the form of steel sheets, smooth steel tubes and biaxially cold deformed steel tubes were made available. The biaxially deformed steel tubes were prepared as indentations of different characteristic widths and depths. The experimental part of this thesis is divided into several experiments and measurements, performed at both Tetra Pak and LTH.

3.1 Material

The material under investigation in the thesis was 316L austenitic stainless steel. This is an FCC, low carbon stainless steel containing nickel- and chromium. 316-type stainless steel is used in high temperature applications such as heat exchangers and parts of engines. 316L is similar with the main difference being lower carbon content, as indicated by letter L. It is better suited for utilization with welding processes due to a lower risk of carbide precipitates good for corrosion resistance. This is a natural choice of material for the steel tubes implemented in processing equipment at Tetra Pak due to the good heat resistance and welding properties. In Figure 3.1 below, mechanical properties of 316-type stainless steel such as the ultimate tensile strength (UTS) and yield strength (YS) are plotted as a function of cold reduction. These values are illustrative as an expected trend for the property evolution in 316L steel used at Tetra Pak and are taken into account when selecting the dimensions of specimens.
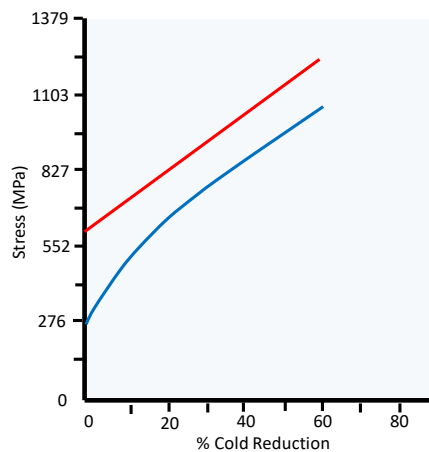
Figure 3.1 Evolution of yield stress (blue) and ultimate tensile stress (red) as a function of cold reduction for 316-type stainless steel. Reproduced from [24]

The as-supplied material was 316L steel in the form of sheets with a thickness of 0.8 mm and a width of 49.7 mm and tubes with a thickness of 0.8 mm and an outer diameter of 16 mm. The tubes were available both in straight and biaxially cold-deformed conditions. The composition of the material, taken from the product specifications of the sheet supplier is shown below in Table 3.1.

Table 3.1: Composition of 316L stainless steel used in the study.

Element	C	Mn	P	S	Si	Cr	Ni	Mo	N	Fe
Composition (wt%)	0.028	0.87	0.035	0.001	0.53	17.00	10.10	2.03	0.032	Balance

The different states of material during the fabrication process of steel tubes used in processing equipment, are shown along with the acquisition of samples in Figure 3.2 below.
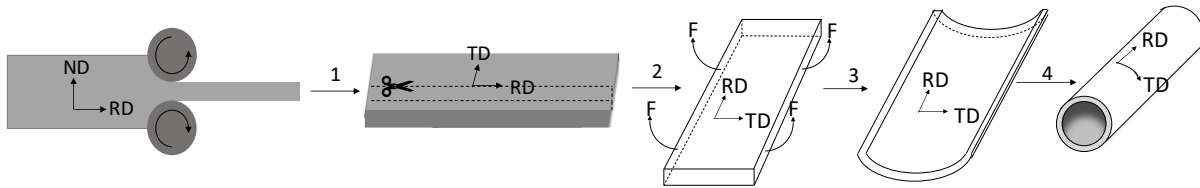
Figure 3.2: Product process from slab to tube. Slabs are cold rolled into sheets (1) that are further cut into strips (2). These strips are bent (3), welded together and heat treated to obtain a tube (4). This product is then delivered to Tetra Pak.

From the Figure 3.2 above, it is seen that the material is processed in several steps, each affecting its properties and microstructure. The sheets and tubes are not manufactured at Tetra Pak, and detailed information about the process was not available. Based on basic knowledge of metal sheet forming process, the following is a fair assumption of the process. At the sheet forming process, as-cast ingots of 316L stainless steel are first hot rolled for the major reduction and then stepwise cold rolled and heat treated until they reach a thickness of 0.8 mm sheets (1). Information on intermediate heat treatment temperatures and if the final cold rolling was followed by heat treatment was not provided but was investigated in the experimental work. If the final rolling occurs at low temperatures without any following heat treatment, the microstructure is affected and the material is work hardened, with dislocations in the lattices and the grains deformed into elongated structures in the rolling direction. However, it may also be annealed to eliminate the work hardening effects and to recrystallize the grains. The sheets are cut into strips of the desired width, 49.7 mm (2). Afterwards, the strips are deformed into a cylinder (3), their long edges are welded together, and heat treated at 1280 °C to produce steel tubes (4). During the process of tube forming, surface roughness can be affected by both cold work when forming the tubes and by the heating of weld and following heat treatment. The weld might work as a form of annealing reducing the effect of previous cold work in the heat affected region. Since the effect of heat from a weld is highest at the fusion zone and decreases while moving away from the fusion zone, there is a chance of a gradient over the tube in both directions originating from the weld line to the opposite site and 180° away from the weld line. The smooth tubes that are formed are then delivered to Tetra Pak where they are implemented in the processing equipment.

3.2   Mechanical testing

To obtain information on the mechanical properties of the material, tensile testing was performed on dog bone-shaped specimens from 316L stainless steel sheets in as-received condition. This data was used as a background for the analysis of correlation between strain and surface roughness. The mechanical testing was performed on at least three specimens at LTH using an Instron E10000.

The specimens were cut from the steel sheet in TD. Their dimensions were slightly scaled down from respective ASTM-8M standard. The gauge length and width were 21 mm and 4.2 mm, respectively. Other dimensions and the justification for their selection can be found in appendix A. Figure 3.3 below illustrates a schematic drawing on the specimens shape [25].
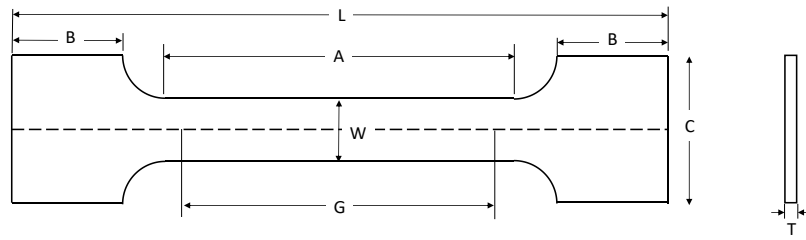
Figure 3.3: Dog-bone specimen. Dimension designations according to ASTM standards, see appendix A. Drawn to scale.

3.3 Roughness related to Strain

To investigate the relationship between surface roughness and strain level, samples were uniaxially deformed to various levels. Surface roughness at different strains was measured using an Alicona IF portable microscope.

These experiments were divided into three different cases. First, one is *unpolished* steel sheets in the as-supplied condition before tube forming. These specimens were tested in RD, TD and 45° in between RD and TD, to investigate anisotropy in 316L with regard to surface roughening. The second case is *polished* steel sheets, also tested in these three directions. Since stainless steel forms a passivation layer on the surface, it is of interest to distinguish between the roughening effects produced by the austenitic crystal- and microstructure and that by the passivation layer. This can be done from the comparison of unpolished and polished sheet surfaces.

The third set of experiments was conducted on tubular sections. Although tubular sections are closer to the real-life scenario at Tetra Pak, steel sheets have a much more convenient shape from the perspective of specimen cutting, polishing and performing tensile tests. Tubular specimens give rise to challenges when it comes to tensile testing in directions other than RD, which is also parallel to the axis of tube symmetry in this case. Equipment for tensile testing along the curvature was not available. Therefore, it was decided to perform the majority of experiments on sheets for obtaining a most critical knowledge. Yet, experiments in RD of tubular sections were also conducted to explore the similarity of trends between surface roughness and strain to the sheet samples.

Unpolished sheet specimens were cut from the supplied steel sheet by using spark erosion. The shape and dimensions of the specimens for mechanical testing were kept the same as listed in Table A.1. They were cut out according to Figure 3.4 below.
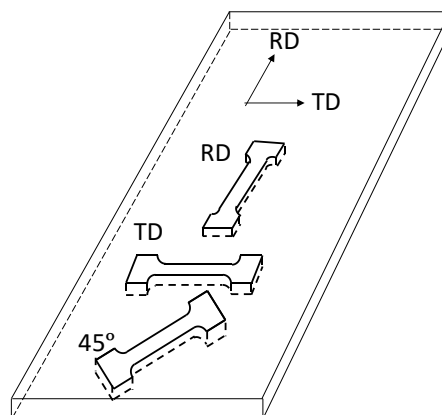
Figure 3.4: Schematic drawing of how the directional samples are cut out from steel sheet.

The polished specimens were cut from a steel sheet using a water-jet cutter. Dimensions and orientations (RD, TD, 45°) of the samples were similar to the unpolished samples. They were then prepared by grinding on SiC paper using Pace Technologies Penta-5000 hand grinder followed by polishing using a Struers Rotopol-22. The last two polishing steps were 0.25 μm diamond suspension and 0.04 μm colloidal silica. To determine the levels of strain to be used in the interrupted tensile tests, the stress-strain curve in Figure 4.1 was analyzed.

The tubes used in processing equipment have a diameter of 16 mm and a thickness of 0.8 mm. The cross-sectional area of a tube is A=38.2 mm^2. Since the maximum force of the tensile machine, F$_{max}$, is 7.5 kN, the maximum possible stress applied on a tube is σ$_{max}$=196 MPa. This is too low to overcome both ultimate tensile strength and yield stress of 316L. It was thus necessary to reduce the cross-section area of the tubes, which was done by cutting them into strips, referred to as tubular sections. The ASTM-8M standard allows cutting the tubes into strips for mechanical testing. The dimensions to be used were determined from the data obtained in the experiments on the sheet samples. It was concluded that cutting the tubes into quarters produces specimen cross-section area small enough to match the maximum force capacity of the instrument. The weld line of each tube was isolated to an individual quarter section, excluded from testing. This was accepted to minimize uncertainties and variance from heterogeneities in the microstructure. According to ISO and the ASTM-8M standard, gripping heads may be flattened when conducting tensile tests on tubular strips, but the curvature of the gauge must remain in the original shape [26]. In these experiments, the gripping jaws flattened the gripping section, but the curvature of the gauge area was maintained.

To obtain the surface roughness parameter, Sa, the measurement area was that of the image field obtained in the 20x magnifying lens, an area of 875 x 655 mm^2. To obtain Ra, the data from 4 mm line scan was extracted. Initial roughness was measured on the unstrained specimens. For the unpolished specimens, Sa and Ra were measured on the sheets from which the specimens were cut out and the average values were used as the initial roughness. For the polished specimens, the average of several measurement from different specimens was used as the initial Sa roughness. It was not possible to measure Ra since the reflectivity of specimen surfaces resulted in essentially no contrast on the optical images. It was not possible to have a 4 mm continuous measurement. Instead the last two polishing dimensions 0.25 μm and 0.04 μm were used as a reference for the initial roughness. The initial roughness of the tubular section was obtained as the average of several measurements of different specimens for both Sa and Ra.

After initial roughness measurements, interrupted tensile testing was performed on the specimens. An experimental set up of the tensile-testing machine is shown below in Figure 3.5.
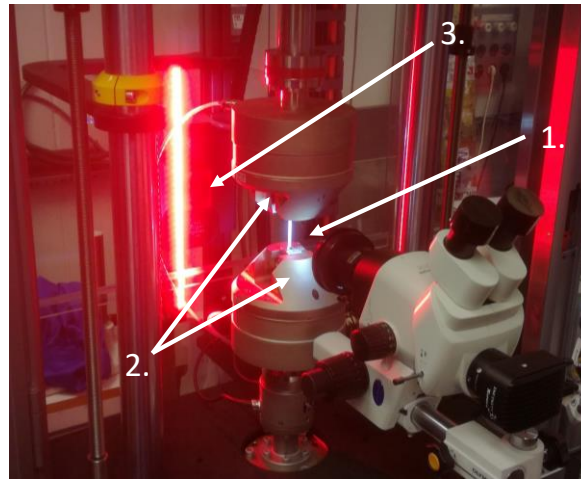
Figure 3.5: Experimental set up based on Instron electropulse E10000 showing the specimen (1), the grips (2) and the video extensometer (3) with white arrows.

In the Figure 3.5 above, different components can be seen. The ends of a sample (1) is clamped in pneumatic grips between two actuators (2) that apply tensile force to the specimen. The red light is used by the video extensometer (3) positioned behind the sample. This is used for measuring the extension of the specimen. By marking the sample with two contrast dots painted in the ends of the gauge length, the video extensometer can follow the displacement of these marks and thus, the specimen extension is captured during the test. In Table 3.2 strain levels and directions in the different sets of samples are indicated by crosses.

Table 3.2: Strain levels used for the different samples.

Engineering strain	Polished sheets	Unpolished sheets	Tubular sections
Directions	RD, TD, 45°	RD, TD, 45°	RD
0.05	X		
0.15	X	X	X
0.225	X		
0.30	X	X	X
0.45	X	X	X
Breakage		X	X

After the specimens were deformed, the surface roughness was measured, and the parameters Ra and Sa were extracted.

3.3.1 Biaxially strained steel tubes

To obtain knowledge of more complex cold deformation process of steel tubes, measurements on indented cold deformed tubes were performed. Figure 3.6 below illustrates how this was implemented.
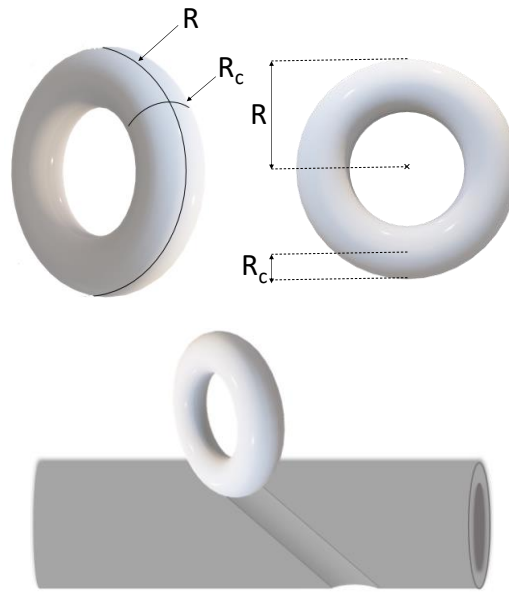
Figure 3.6: Schematic drawing of deformation wheel with the two different radii indicated (upper) and an illustration of how a wheel forms the indentation of a tube (bottom). Not drawn to scale.

As is shown in the figure a wheel in the shape on a torus with an impeding force plastically deforms the tubes resulting in a deformation pattern. The two different radii of the torus are designated as R, which is the radius across the entire torus, and R_C, which is the radius of curvature. The measured tubes had indentations with different depths and radii of curvature of the wheel. These parameters are summarized in Table 3.3 below. The specimen designation used is RxDy, where x and y indicate the radius of curvature of the wheel and the depth of imprint in millimeters respectively.

Table 3.3: Table of parameters for cold deformed tubes.

Specimen	Depth (mm)	Radius of curvature (mm)
R4D1	1	4
R2D0.4	0.4	2
R12D0.8	0.8	12
R7D0.8*	0.8	7
R12D0.4	0.4	12

*The R7D0.8 specimen was processed differently and had a much narrower spacing between the spiraling pattern than the other specimens.

All the specimens were prepared from tubes with an outer radius of 16 mm and a thickness of 0.8 mm. Since the internal surface of the tubes were of prime interest, they were cut in half to perform the measurements. Both Ra- and Sa-values was measured. For the Ra-values a 4 x 4 mm^2 stitch was performed and then data from 4 mm long vertical (RD) and horizontal (TD) lines were obtained to determine Ra in these directions. For the Sa-values the size of the area measured was the one of the image field obtained when using the 20x magnifying lens, which is 875 x 655 mm^2. The data was extracted from both single image fields and from the stitched measurements, using a measurement area of the same size as the 20x image field.

Since there is a risk that the roughness between tubes can differ slightly before the deformation process, it was decided to measure both the non-deformed (denoted smooth in the report) area of the

specimens and on top of the deformations for each tube. The difference between these is of prime interest. Such separate measurements ensure the distinction of roughness specific to deformation.

To correlate the surface roughness to strain, two different models were used for to obtain a value of the strain of indentations. One, a 1D strain calculation parallel with the steel tube and the other, a model developed by FS Dynamics using FEM to simulate equivalent plastic strain PEEQ strain during the deformation process.

3.4   Microstructure characterization

As mentioned above in subsection *2.2.2 effect of microstructure*, earlier studies show that surface roughness is affected by grain size. In the case of a linear relationship between surface roughness and true strain, a linear relationship between roughening rate and grain size seems to take place. It is thus of interest to measure grain dimensions in the directions of sheet deformation. This will allow investigating the correlation between grain dimensions and the roughness-strain data extracted from the experiments discussed in subsection *3.3 Roughness related to Strain*. The grain size measurements were conducted using TSL-OIM EBSD system integrated into an E-SEM FEI Quanta 200 MKII available at the Division of Materials Engineering in LTH. EBSD measurements were used to extract information on grain dimensions, the microstructure and the orientation of grains. The average distance between grain boundaries (grain boundary intercept length) was measured in RD and TD. The specimens used for the analysis had rectangular shape with the RD-TD plane parallel to the measurement surface. Several scans were performed in different locations of the specimen. The area of each EBSD scan was 150 x 630 µm², and the step size was 1 µm. This procedure of specimen preparation for the EBSD analysis was the same as for the polished sheet specimens of subsection *3.3 Roughness related to strain.*

For SEM imaging, three different imaging modes was implemented. One was using a secondary electron (SE) detector. In this mode, the signal originates from detecting electrons knocked out from the sample caused by the momentum of the initial electron beam. This mode gives rise to primarily edge- and topological contrast, with some elemental contrast obtained as well. The other modes were both from using a backscattered electron (BSE) detector, operated either in topological mode or in elemental mode. As suggested by the name, topological mode is sensitive towards topology with this as the primary contrast source. Elemental mode gives rise to chemical contrast (or z contrast) and is mainly sensitive towards the chemistry of the sample, but is also well suited to distinguish grains and twinning.

SEM images was taken on the RD-TD surface of both a polished and an unpolished dog-bone specimen at zero strain and after straining them to 30 percent elongation. SEM images were taken also on the RD-ND (normal direction) plane and the TD-ND plane by cutting out rectangular samples according to Figure 3.7.
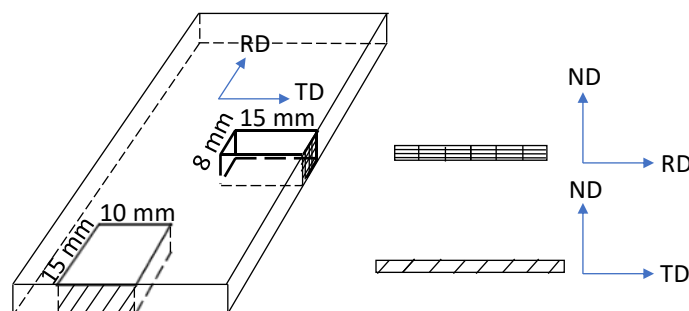
Figure 3.7: Schematic figure of specimens cut out from steel sheet for RD-ND and TD-ND SEM imaging.

The figure above show how two specimens are cut out from the sheet to obtain the desired planes for imaging. The dimensions of the specimens were chosen with respect to sample holders available and for the reason of distinguishing them from each other. The experiments were conducted to acquire qualitative information of microstructure.

To characterize the difference between the surface of unpolished and polished sheets, EDS was performed. For both a polished sample and an unpolished sample, five point analyses were conducted using an acceleration voltage of 20 keV. The unpolished specimen was tilted by 75° to enhance the response from the surface.

Using equation (7) together with the composition found in Table 3.1, M_d for the material can be calculated to M_d=7.0 °C. This indicates that the formation of strain-induced martensite might be possible even at room temperature and therefore it was of interest to analyze the phase composition. The amount of martensite was measured by EBSD using the analytical system Pegasus (EBSD+EDS) from EDAX which is incorporated in an environmental SEM of type FEI Quanta 200 MKII. At first, the concentration of martensite was measured for an unstrained steel sheet specimen. The specimen was then strained to ε=0.30 and measured again.

4 Experimental results and analysis

This section is dedicated to results from the experiments as well as discussion and analysis of results.

4.1 Mechanical testing

Figure 4.1 below show stress-strain curves from tensile tests of two TD specimens.
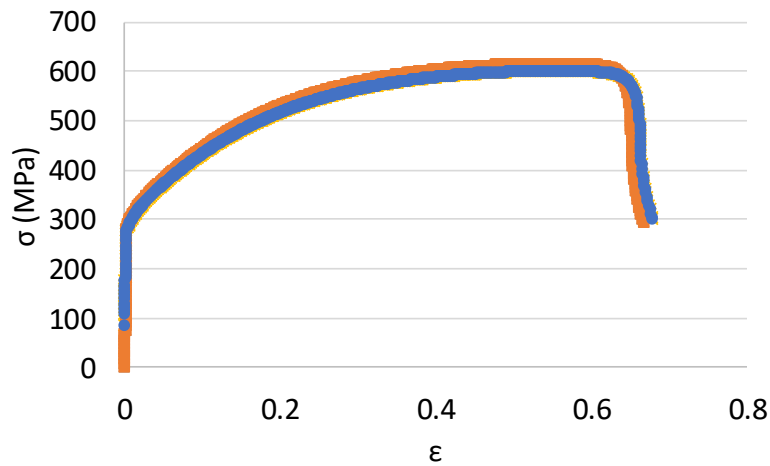
Figure 4.1: Engineering stress-strain curve for tensile tests of 316L sheet samples in transverse direction. Two curves are shown to demonstrate reproducibility.

From this data, the ultimate tensile stress is found to be approximately 630 MPa, the yield stress 250-275 MPa, and the E-modulus 150-180 GPa. The yield stress and UTS also correlates well with that in Figure 3.1 for 316 steel without cold reduction, indicating that this is the state of the as-supplied material in this investigation.

4.2 Surface roughness related to strain

Surface roughness was measured for specimens sampled at different steps of deformation. The following sections present the results and data together with respective analysis.

4.2.1 Polished sheets

The strains at which the polished specimens were tested are tabulated in Table 4.1.

Table 4.1: Table listing the engineering strain levels for the polished specimens.

Specimen	1	2	3	4	5	6
RD	0	0.0489	0.150	0.225	0.326	0.449
TD	0	0.0478	0.150	0.226	0.300	0.450
45	0	0.0482	0.150	0.225	0.343	0.421

The strain levels were calculated as the difference between final and initial lengths divided by the initial length.

Below in Figure 4.2, the six specimens strained in TD are shown from left to right.
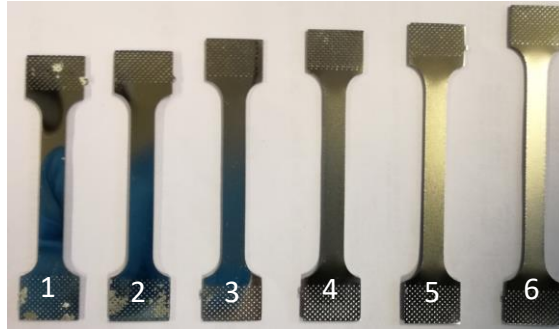
Figure 4.2: Overview of the six TD specimens (1-6 from left to right) from the interrupted tensile testing.

The results from surface roughness measurements of the RD samples are plotted against the true strain for Sa and Ra in Figure 4.3.

Figure 4.3: Dependence of surface roughness on true strain for polished specimens deformed in RD: (a) surface average, Sa and (b) line average, Ra (black) together with the grain size of abbrasive particles in the last two polishing steps (red). Standard deviation is indicated by the error bars. The numerical values of the data points can be found in Appenix B.

From the figure above, one can observe a positive correlation between roughness and strain for both Sa and Ra at the lower strain levels. At an engineering strain of 0.15 both Sa and Ra reach their maxima, and then decrease in a dependence resembling logarithmic law. As mentioned earlier, due to high reflectivity of the initial undeformed sample surfaces, an uninterrupted line of 4 mm was not possible to capture using the 3D-optical microscope. Therefore, it was assumed that the initial line roughness, Ra, in such specimens is in between the abrasive particle size in the two final polishing steps, i.e. 0.04 μm and 0.25 μm, as indicated by red circles in Figure 4.3b. This appears as a reasonable assumption when comparing with the zero-strained Sa-roughness of 0.163 μm in Figure 4.3a. Both are in approximately the same size range. The trends presented in Figure 4.3 disagree with earlier results in the literature [5-8] where monotonically increasing linear relationship was reported.

The results from the analysis of TD specimens is presented below in Figure 4.4.

Figure 4.4: Dependence of surface roughness on true strain for polished specimens deformed in TD: (a) surface average, Sa and (b) line average, Ra (black) together with the grain size of abbrasive particles in the last two polishing steps (red). Standard deviation is indicated by the error bars. The numerical values of the data points can be found in Appenix B.

Figure 4.4 reveals that the TD specimens follow the same trend as the RD specimens: roughness increases at low strain, then reach a maximum surface roughness peak at ε=0.15, following a decrease to ε=0.45.

The samples deformed at 45° angle to RD are shown in Figure 4.5 below.

Figure 4.5: Dependence of surface roughness on true strain for polished specimens deformed in in 45° to RD: (a) surface average, Sa and (b) line average, Ra (black) together with the grain size of abbrasive particles in the last two polishing steps (red). Standard deviation is indicated by the error bars. The numerical values of the data points can be found in Appenix B.

Figure 4.5 demonstrates again the trends similar to the RD and the TD samples. An increase in roughness at low strains, maximum surface roughness at ε=0.15, and a decrease in surface roughness afterwards. The only exception from otherwise similar trends is the last data-point at ε=0.45 showing a minute increase in the surface roughness. This might be caused by the localization of strain in the specimen, which developed severe necking and fractured at ε=0.42. Therefore, surface roughness might be affected by the additional localized strain of grain rotation due to elastic strain recovery.

Specimens within the TD sample developed the highest surface roughness for both Sa and Ra within the strain levels investigated, while RD sample has the lowest surface roughness, and the 45° sample lies in between. All the sample sets show the same trend of an increasing roughness at low strain levels, reach a peak, and then decreases towards a saturation level in a dependence resembling logarithmic law. A feasible explanation for such a trend is local grain rotation aimed at accommodating crystallites of different orientations. As explained in subsection *2.1*, grain rotation caused by a primary slip system occur until reaching a steady state where a secondary slip system has the same amount of critical resolved shear stress. However, the rotation has a slight overshooting phenomenon where the initial rotation goes past the steady state before rotating back. This can explain the evolution of roughness in the diagrams above. Specifically, the initial positive part of the strain-roughness relationship takes place until overshooting. When the secondary system activates, the grains rotate back thus reducing the surface roughness to a point where multiple slip systems become active.

4.2.2 Unpolished sheet samples

The engineering strain levels to which the unpolished specimens were deformed in interrupted tensile testing are summarized in Table 4.2.

Table 4.2: engineering strain levels in the interrupted tensile testing of unpolished SS316L steel samples.

Specimen	1	2	3	4	5
RD	0	0.143	0.303	0.447	0.558
TD	0	0.143	0.309	0.452	0.58
45	0	0.151	0.313	0.451	0.592

In Figure 4.6, all the stress-strain curves of the RD samples used in the interrupted tests are presented in one diagram. The diagram reveals almost perfect reproducibility of results.
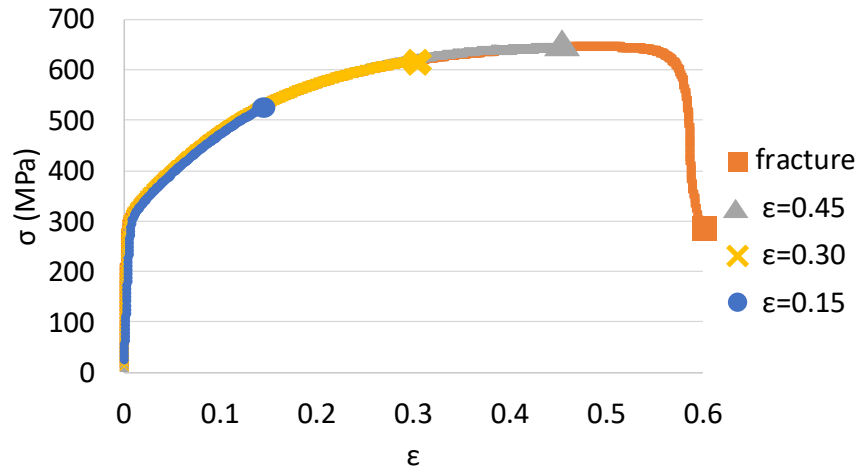
Figure 4.6: Representative stress-strain curve of unpolished RD specimens 2-5 Table 4.2. Markers represent the final strain in the interrupted tensile tests.

The arithmetical surface- and line roughness for each of the directions vs true strain are shown in Figure 4.7-Figure 4.9 below. The numerical values of data points can be found in appendix B.
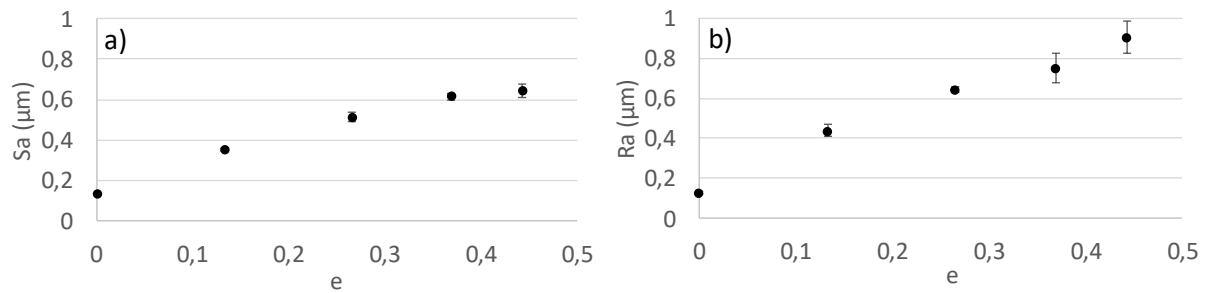
Figure 4.7: Dependence of surface roughness on true strain for unpolished specimens deformed in RD: (a) surface average, Sa and (b) line average, Ra. Standard deviation is indicated by the error bars.
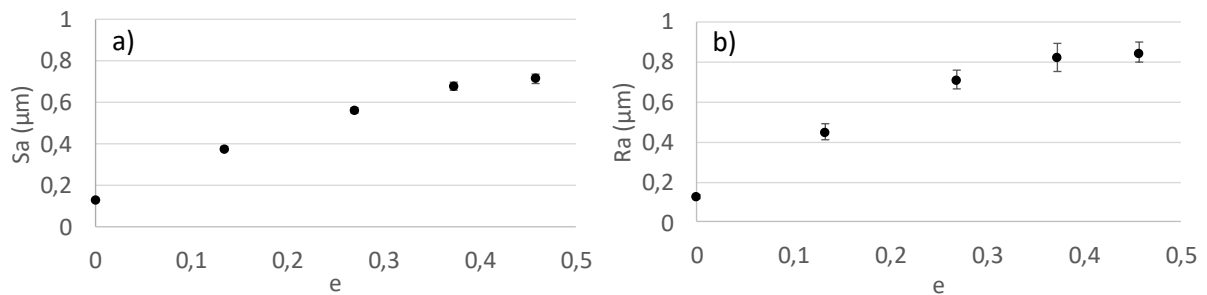
Figure 4.8: Dependence of surface roughness on true strain for unpolished specimens deformed in TD: (a) surface average, Sa and (b) line average, Ra. Standard deviation is indicated by the error bars.
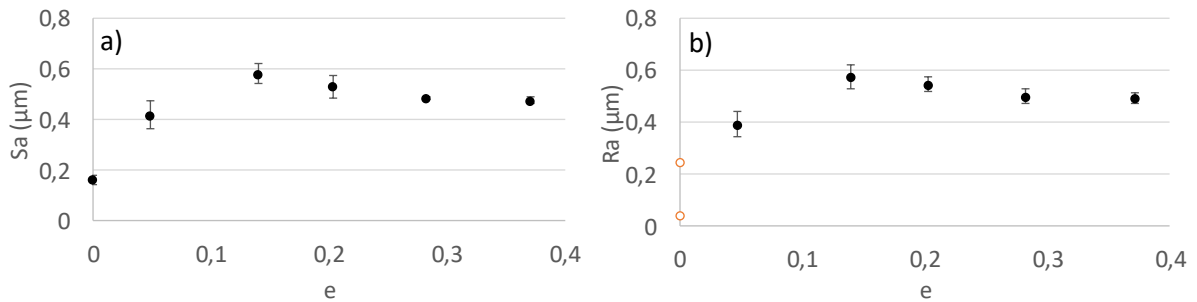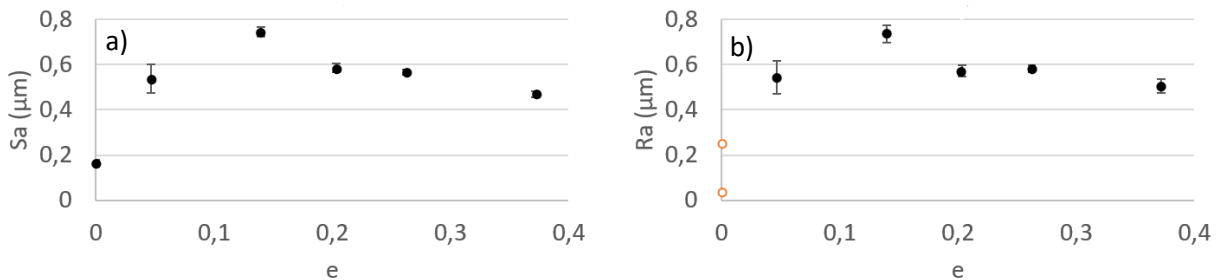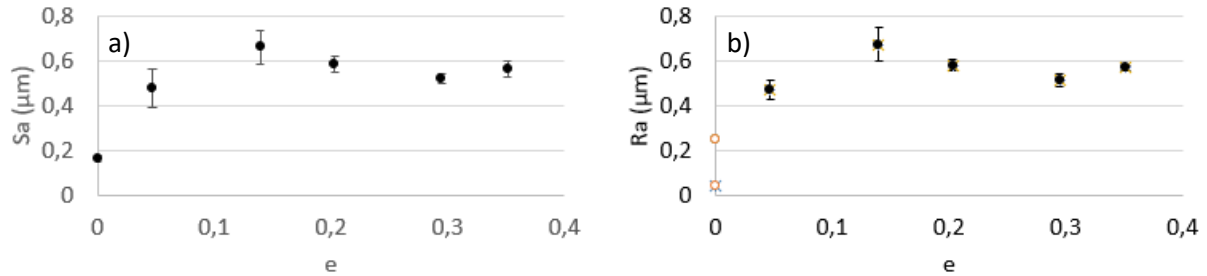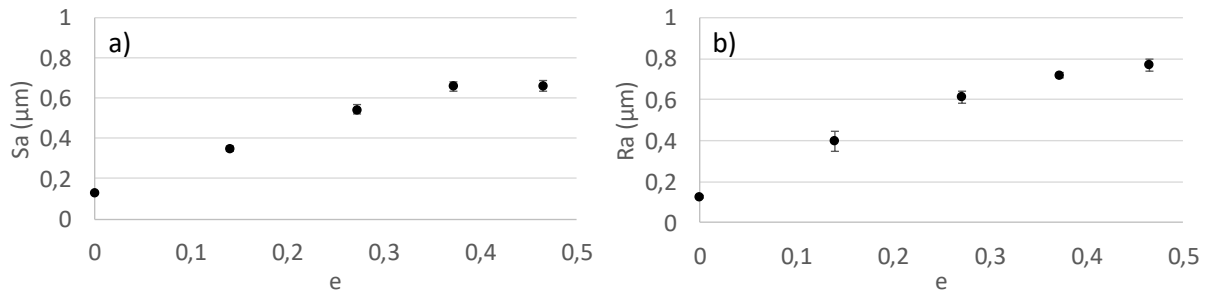
Figure 4.9: Dependence of surface roughness on true strain for unpolished specimens deformed in 45°: (a) surface average, Sa and (b) line average, Ra. Standard deviation is indicated by the error bars.

These results reveal a significant difference with the polished samples. In Figure 4.7-Figure 4.9, the correlation between strain and surface roughness is consistently positive (monotonically increasing) for all the unpolished samples. By first comparing the Sa-e diagrams in Figure 4.7-Figure 4.9 for the different directions, it appears that the specimens 1-4 (ε=0-0.45) have a linear trend, i.e. an increase in surface roughness with increasing strain. This is in a very good agreement with the results found in the literature survey. At the same time, they might be interpreted as quadratic. However, the fifth data points deviate from these trends indicating a dramatic reduction in roughness increase rate. For the 45° specimens, surface roughness appears even lower at fracture than at ε=0.45. Such a trend change can be explained by saturation, i.e. the decreasing strain effect on roughness. However, it is more likely due to strain localization or necking and the reduction of specimen thickness near fracture. When necking starts to appear, elongation takes place in the necking area only. Since roughness measurements were performed far away from the neck area, it is possible that the actual strain level in that area was lower than the average specimen strain calculated from total elongation. Thus, the slope of Sa − e relations appears declining while strain levels at the last datapoints are actually overestimated. In the data from tensile testing, engineering strain at UTS was measured to be ε=0.5 (or a true strain of e=0.41). Hence, the strain level at the area of roughness measurement for the fifth data point is presumably e=0.41, which correlates much better with the trend of the other data points. Due to these uncertainties in the strain levels of specimen 5 in all the directions, respective data points were excluded from modeling the relationship.

For Ra-values, similar trend can be found with the exception of RD data, where the increase from ε=0.45 to fracture seem to be larger than the average increase. Note that those two data points have rather large standard deviation. For TD and 45° samples, the relationship between Ra and e seem to be close to linear up to ε=0.45, similar to the Sa samples.

For the further analysis of the Sa − e relationship, linear and second-degree polynomial fits were applied for the first four experimental data points. These are shown for RD in Figure 4.10 together with the residual plots and R^2-values.

Figure 4.10: Dependence of surface roughness on true strain for unpolished specimens deformed in RD. a) Sa versus true strain with linear regression (solid red) and second-degree polynomial (dashed blue) for the first four data points with respective equations. b) residual plot for the linear Sa-e regression. c) residual plot for the second-degree polynomial Sa-e regression. Note the difference in scale between residuals. d) Ra versus true strain with linear regression (red) and second-degree polynomial (blue) for the first four data points with respective equations. e) residual plot for the linear Ra-e regression. f) residual plot for the second-degree polynomial Ra-e regression.

Figure 4.10a above clearly demonstrate that both the regressions fit the Sa-e data quite well. The residuals for both respective regressions are very small compared to the size regime of surface roughness, see Figure 4.10b and c. Characteristic properties of a residual plot for a well-suited fit are not only small values but also random distribution. This would be difficult to analyze with such few data points. Therefore, it is more appropriate to analyze the residuals from separate residual plots. Doing this for the Ra-e data in Figure 4.10d-f, very similar patterns is found in the residuals. In the residuals of linear regression of both the Sa and Ra data, Figure 4.10b and e, the first and last data points are negative, and the two intermediate points are positive. This always occur if a linear trendline is fit to a four-point negative quadratic data set. Residuals for the linear regression are thereby an indication that a quadratic fit is more appropriate. For Ra, the quadratic relationship seems to fit much better than the linear one, Figure 4.10d. Nevertheless, it should be noted that the standard deviation of the last data point is very large. From the residuals of the quadratic fits, it also appears to be a trend that both residual plots have a zig zag pattern. However, the residuals are very small, which is a clear indication of a good fit. One can also examine the R^2-values that equal to 0.988 for the linear fit and unity for the quadratic fit of the Sa data. Although the R^2-value equals unity, it should not be overvalued because of the low number of experimental data points in the set. If a data set has only three points, it is always possible to find a perfect second-degree polynomial fit. Four data points are therefore too few to use R^2-values as the absolute proof of a good fit. The goal in this case is rather to see if the R^2-value is low, which could have been used as proof for a poor fit. Just by looking at the trend-line, it can

be said that it appears more quadratic than linear. However, both the regressions fit the data quite well producing very small residuals.

For further analysis and examination of the relationship between surface roughness and strain, the results from RD specimens are compared to the samples of the other directions, starting with the TD specimens shown in Figure 4.11 below.
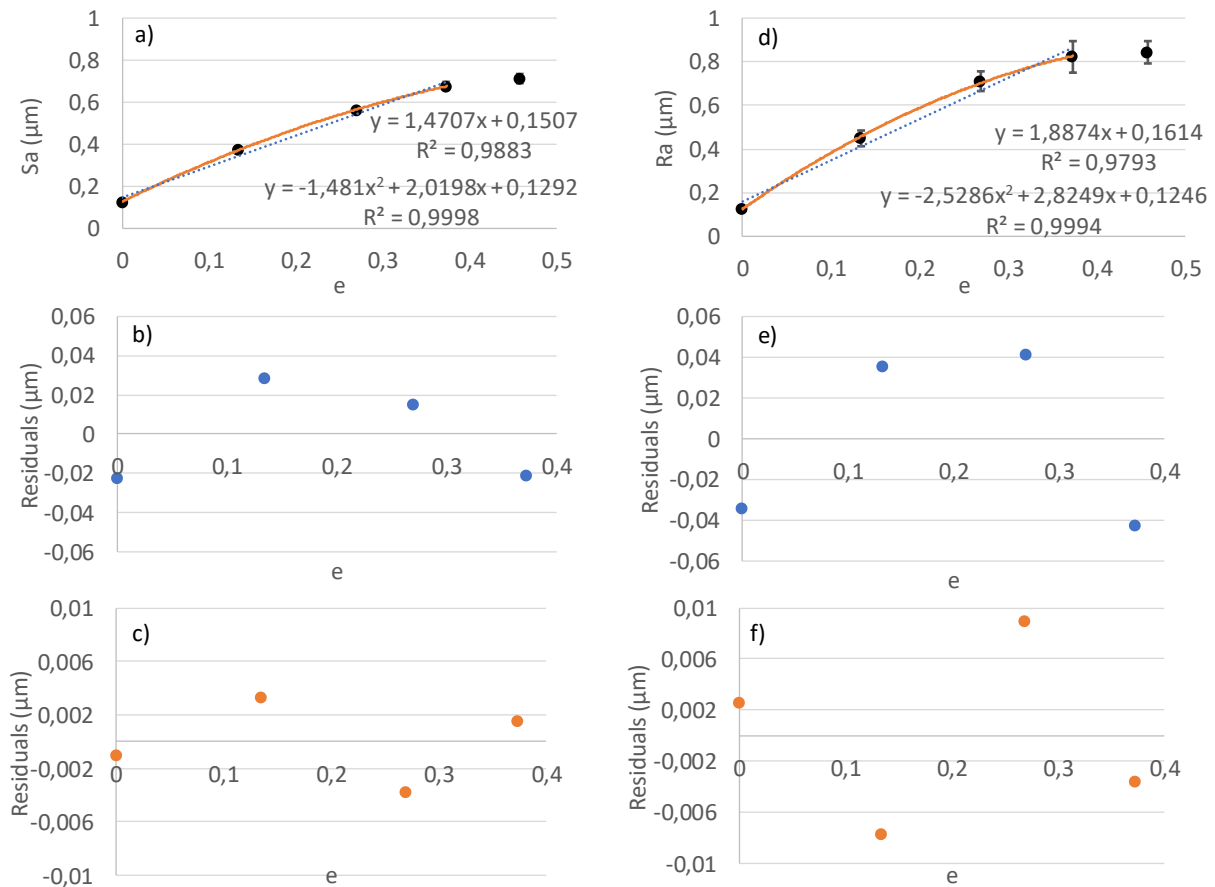
Figure 4.11: Dependence of surface roughness on true strain for unpolished specimens deformed in TD. a) Sa versus true strain with linear regression (solid red) and second-degree polynomial (dashed blue) for the first four data points with respective equations. b) residual plot for the linear Sa-e regression. c) residual plot for the second-degree polynomial Sa-e regression. Note the difference in scale between residuals. d) Ra versus true strain with linear regression (red) and second-degree polynomial (blue) for the first four data points with respective equations. e) residual plot for the linear Ra-e regression. f) residual plot for the second-degree polynomial Ra-e regression.

The Sa-e data in the Figure 4.11 above correlates quite well with both the linear and the quadratic trendlines. However, similar to the RD samples, residuals in the quadratic fit, Figure 4.11c are approximately 10 times smaller than those in the linear one, Figure 4.11b. The Ra-e data has an even clearer trend towards quadratic relationship, Figure 4.11d. Nevertheless, it should be noted again that although residuals are remarkably smaller for the quadratic fit, they are still very small even for the linear one. Quadratic fit always has smaller residuals (or equally small for perfect linear data). However, the factor of ten difference is significant. The linear fit residuals have the same appearance for both the Sa- and Ra-data for both RD and TD. Therefore, it is possible to state now that the residuals follow a trend and are not randomly distributed. For the quadratic regression, it is still ambiguous. The Sa quadratic residuals of Figure 4.11c are similar to those of the Sa quadratic residuals in Figure 4.10c and f. However, quadratic residuals of Ra in Figure 4.11f have different distribution. Regardless of using a linear or a quadratic model to describe the relationship, the inclination of curve is larger in TD, with a RD:TD ratio of approximately 1:1.1.

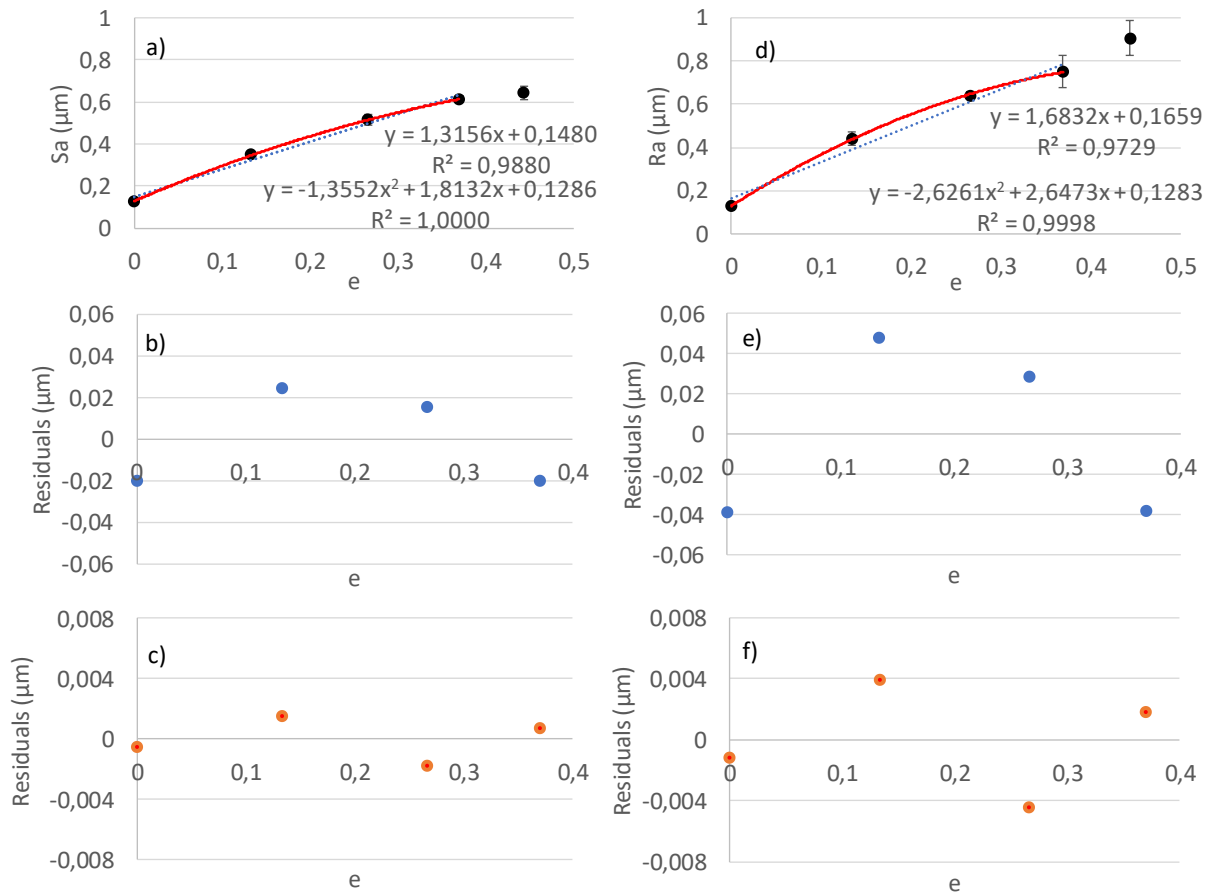The 45° samples trendlines and residuals are plotted below in Figure 4.12.
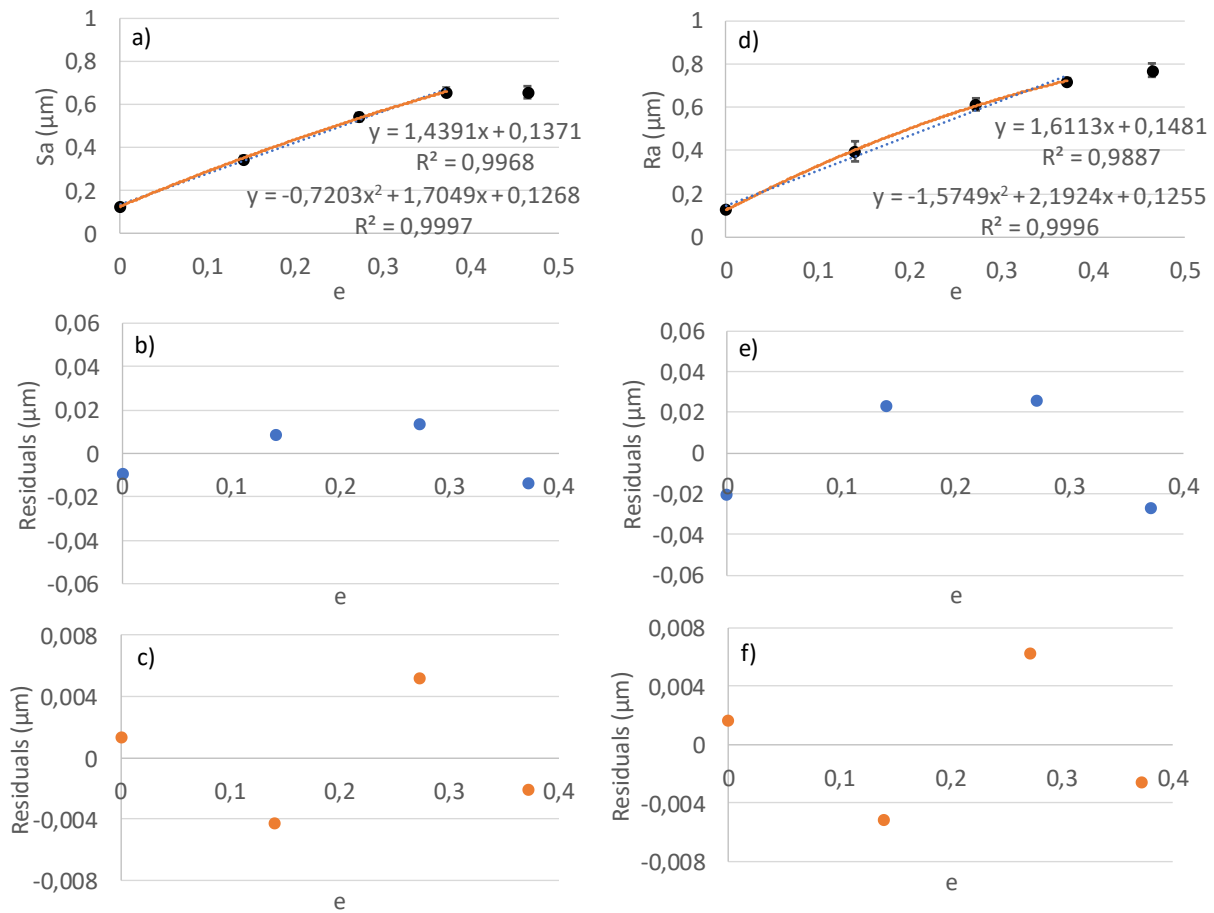
Figure 4.12: Dependence of surface roughness on true strain for unpolished specimens deformed in 45°. a) Sa versus true strain with linear regression (solid red) and second-degree polynomial (dashed blue) for the first four data points with respective equations. b) residual plot for the linear Sa-e regression. c) residual plot for the second-degree polynomial Sa-e regression. Note the difference in scale between residuals. d) Ra versus true strain with linear regression (red) and second-degree polynomial (blue) for the first four data points with respective equations. e) residual plot for the linear Ra-e regression. f) residual plot for the second-degree polynomial Ra-e regression.

Both the trendlines shown in the Sa-e data of Figure 4.12 above correlate well. Besides the first data point, they both are within the standard deviation of the experimental data in Figure 4.12a. The residuals shown in Figure 4.12b and c follow similar trends as those in RD and TD samples. Namely, the linear residuals possess the characteristic set of two negative values at the ends and positive in between, and the quadratic residuals possess a zigzag pattern starting with a positive value similar to the Ra-e residuals of TD in Figure 4.11f. For the regression lines of Ra-e data, the linear fit is not as applicable, while the polynomial fit correlates well, Figure 4.11d. The residuals in Figure 4.11e and f have the dependence similar to the Sa-e data.

By comparing the trendlines and residuals along with Sa and Ra for samples in all the directions, it becomes evident that quadratic fit is more appropriate. In the quadratic residuals, all sample sets show a zigzag pattern around zero centerline. Yet, the residuals are very small for both the trendlines, with the percentage (linear) and the permille (quadratic) of the scale of roughness values. The vertical resolution of Alicona microscope is supposed to be 20 nm, and most residuals (all for the quadratic fit) are lower than that. Thus, both the models seem to be applicable, with the quadratic one being a bit more precise. Considering that most residuals in the linear regression are smaller than the resolution

of the microscope, it is fair to say that it is suitable to use in the model of cold deformation process for simplicity. However, the quadratic model can also be used if higher precision is necessary.

4.2.3   Steel tubes

Following section present results and analysis from the tensile testing and surface roughness measurements on the tubular sections. Five different specimens after tensile testing are shown below in in Figure 4.13.

Figure 4.13: Image of the five tubular specimens ordered from zero strain to fracture.

The data from the measurements is presented below in Figure 4.14. Values of individual data points is found in Appendix B.
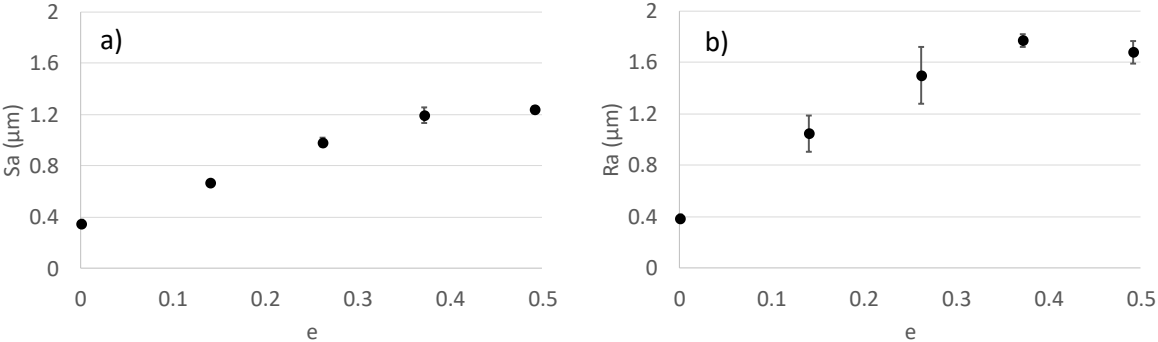
Figure 4.14: Dependence of surface roughness on true strain for tubular section specimens: (a) surface average, Sa and (b) line average, Ra. Standard deviation are indicated by error bars.

A trend similar to the unpolished sheets can be seen for both Sa and Ra in the diagrams of Figure 4.14 above. The first four data points, up to $\varepsilon=0.45$, seem to follow a linear relationship while the fractured specimens show lower surface roughness values then expected from the linear trends. The reason for which is similar to that of sheet specimens, as explained in subsection 4.2.2. When necking starts, essentially all elongation takes place in the necking area. Since roughness measurements are conducted away from the necking area, the strain of the measuring area is lower than the average specimen strain. The true strain at UTS for specimen 5 was e=0.43, suggesting that as the actual true strain of the measurement area rather than e=0.49 indicated in the diagram. A linear regression for the first four data points of the Sa and Ra measurements is shown with respective equation in Figure 4.15.
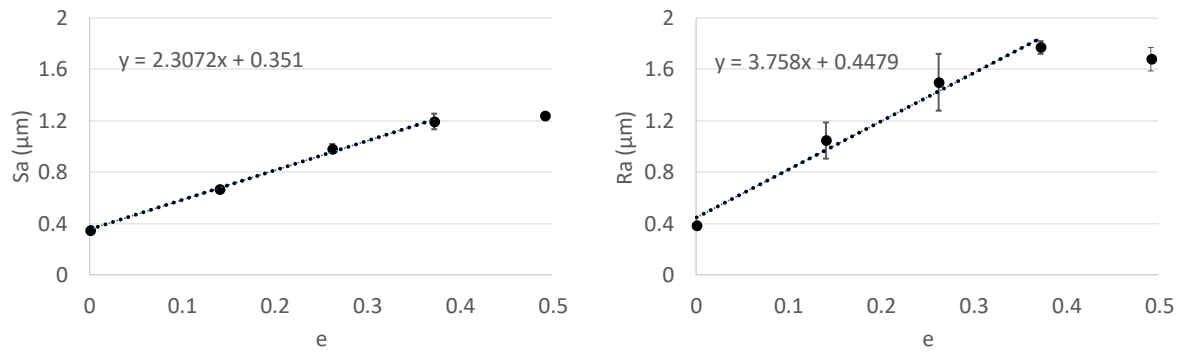
Figure 4.15: Dependence of surface roughness on true strain for tubular section specimens: (a) surface average, Sa and (b) line average, Ra. with a linear trendline overlay. Standard deviations are indicated by error bars.

In the diagrams above it can be seen that the data of the Sa-e plot follow a linear trend very well. The Ra-e diagram does not seem to follow the linear regression line as nicely, but the trendline is still within the SD error bars. The roughness increase rate in the curves is larger than that in the unpolished sheets. The straining of tubular sections in RD generates roughening rates of α_{Sa}=2.31 and α_{Ra}=3.76 while those in the unpolished sheets are α_{Sa}=1.32 and α_{Ra}=1.68. This might suggest that after tube forming and heat treatment, the material properties are modified to change the roughening rate. However, specimen preparation and mechanical testing of tubular sections have some uncertainties potentially affecting these results. As mentioned earlier, the specimens could not be cut according to standards with a wider gripping section than the gauge section. Also, the width of the specimens could not be cut with high accuracy leading to the deviations of width in the gauge ends for some specimens. In addition, the curvature of the specimen leads to bulging during elongation. The consequence of this is a *de facto* biaxial strain, while strain in one dimension was recorded only. Because of these uncertainties no firm conclusions about higher surface roughening rate in tubular sections should be made at this stage. However, this is a topic to be further investigated using more accurate specimen cutting according to standards and biaxial strain measurements. Nevertheless, even if roughening rate cannot be determined accurately, the data shows that the relationship appear linear indicating that a linear model seem to be applicable not only for sheets but also for steel tubes.

4.2.4   Biaxially strained steel tubes

The results from surface roughness measurements of the indented tubes are shown in Table 4.3, normalized against Sa-smooth of specimen R4D1, where specimen designations are the same as those in subsection *3.3.1 Biaxially strained steel tubes.*

Table 4.3: Surface roughness measured for various biaxially strained specimens, normalized against specimen R4D1.

Specimen	Sa-smooth	Sa-indent	Ra-RD-smooth	Ra-RD-indent	Ra-TD-smooth	Ra-TD-indent
R4D1	1	2.60	1.03	6.60	1.32	5.74
R2D0.4	1.00	2.19	1.03	8.77	1.26	6.19
R12D0.8	1.01	2.19	0.85	2.80	1.27	3.29
R7D0.8	1.81	1.75	3.82	3.60	1.90	6.38
R12D0.4	1.05	1.51	1.00	1.87	1.37	2.09

Each reported value is the averages of five measurements. Sample R7D0.8 in table 4.3 seems to have a larger surface roughness on the smooth part than on the deformed part. From the microscopy observations, it became evident that due to the short distance between deformed parts in this specimen (1.3 mm compared to 2.5 mm in the other specimens), the areas between indentations is

also affected. Hence, the Sa- and Ra-smooth values for sample R7D0.8 are not representative of an unstrained area roughness. Yet, it reveals an interesting observation that the indentations affect the area in-between when too frequent.

To determine how cold deformation affects surface roughness, the ratio between strain and surface roughness is compared. In case of a linear relationship between surface roughness and strain, considering that all the specimens are of the same material, the slope of the relationship should be the same for all of them. To evaluate this, first the rather simple 1D model for strain calculation in a steel tube was used. Main assumptions of this calculation are (i) the deformed parts of the tube accept the exact form of the deformation wheel, (ii) strain is very local occurring only when in contact with the wheel, and (iii) strain is evenly distributed over the whole deformation zone.

Schematic of a short tube section before and after cold deformation is shown below in Figure 4.16.
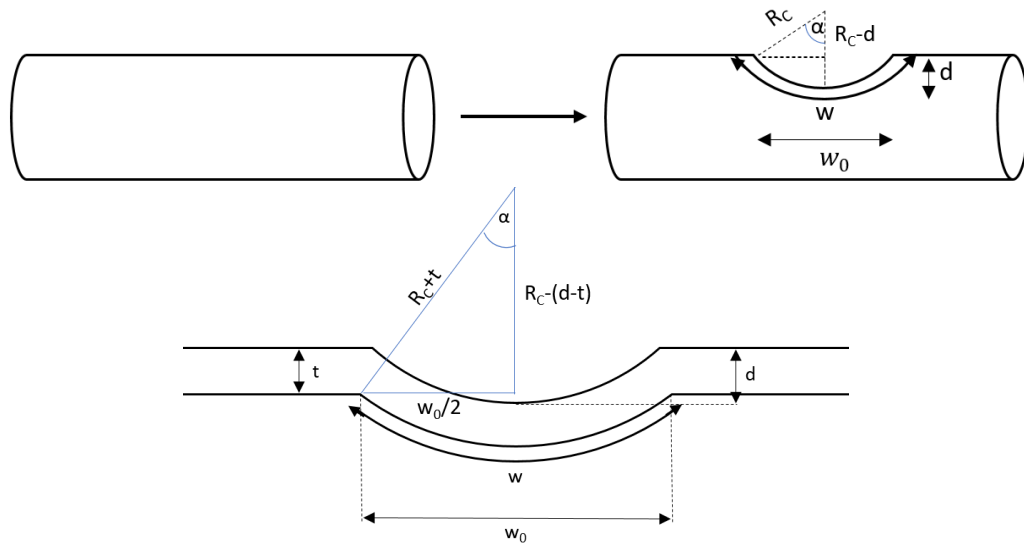
Figure 4.16: Schematic of a small tube section before and after cold deformation.

The known parameters in the figure above are t, which is the tube thickness, d, the indent depth and R_C the radius of curvature of the deformation wheel. w_0 and w are the initial and final lengths of the deformed part of the tube. They can be calculated from knowing the other parameters, which can be then used to calculate engineering strain using the sets of equations shown below.

$$w_0 = 2 \cdot \sqrt{(R_c^2 + t) - (R_c + t - d)^2}$$

$$\alpha = \arccos\left(\frac{R_c + t - d}{R_c + t}\right)$$

$$w = \frac{2\alpha}{360°} \cdot 2 \cdot (R_c + t) \cdot \pi = \frac{(R_c + t) \cdot \pi}{90°} \cdot \arccos\left(\frac{R_c + t - d}{R_c + t}\right)$$

$$\varepsilon = \frac{w - w_0}{w_0}$$

The equations above along with equation (6) allow calculating engineering and true strains for all the indented tube specimens. Calculated strains are tabulated in Table 4.4.

Table 4.4: Engineering and true strains in the biaxially deformed specimens.

Specimen	R4D1	R2D0.4	R12D0.8	R7D0.8	R12D0.4
Eng. strain, ε	0.076	0.051	0.021	0.036	0.011
True strain, e	0.073	0.049	0.021	0.035	0.010

If the cold-deformed tubes follow a linear relationship between true strain and surface roughness, intersection of dependencies of surface roughness in the strained and the smooth parts on true strain represent the relationship. The smooth part of the tube is used as a zero-strain reference. Since the smooth part of specimen R7D0.8 is affected by deformation, the average of Sa-/Ra-smooth value from the other specimens is used for this sample. Figure 4.17 below shows diagrams for the dependence of surface roughness on true strain in the indented tubes for Sa and Ra in RD. Since the strain calculation is one-dimensional in RD the relationship between Ra-TD and e is not analyzed for this model.
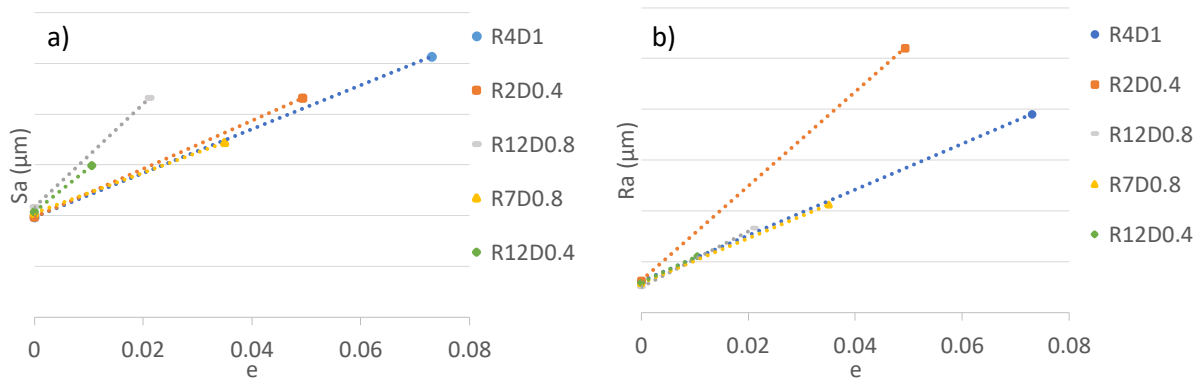
Figure 4.17: Surface roughness related to true strain with linear regression: (a) Sa and (b) Ra in RD.

The values of the slopes relative to specimen R4D1 is tabulated below in Table 4.5.

Table 4.5: Relative values of slopes of the roughness-true strain relationship in biaxially strained steel tubes.

Specimen	R4D1	R2D0.4	D12D0.8	R7D0.8	R12D0.4
Sa	1a	1.10a	2.35a	0.93a	1.99a
Ra	1b	2.06b	1.21b	0.98b	1.09b

In the Sa measurements, it is seen that specimen R4D1, R2D0.4 and R7D0.8 develop relatively equal slopes while specimens R12D0.8 and R12D0.4 deviate significantly from the others. It should be noted that the deviating samples are those with the lowest strains and the largest radius of curvature in the deformation wheel. The strain calculation used here takes into account elongation in one direction only, RD. For the larger radii of curvatures, the elongation in TD increases relative to the elongation in RD. Therefore, the 2D parameter, Sa, is affected more by strain in TD. Hence, the 1D strain calculation might become unreliable for anticipating the Sa value at larger radii of curvature. Another factor affecting the results might be the recovery of elastic strain component upon unloading, which is relatively more significant at lower plastic strain values but is out of consideration in the model.

Looking at the Ra-RD ratios, four out of five specimens have relatively equal slopes while the fifth, R2D0.4, possess a much larger slope. However, the measurements of this specimen had at least two known complications. One is that this is the thinnest indentation studied here. When using the measurement length of 4 mm according to the standard, it covers more than the cold-deformed area only. In practice, it is expected to result in a lower roughness and slope. The second even more significant problem in this case is the surface slope correction in the software. As can be seen in Figure

4.18a below, the profile is not fully filtered out, which has a significant effect on the result, as illustrated in Figure 4.18b
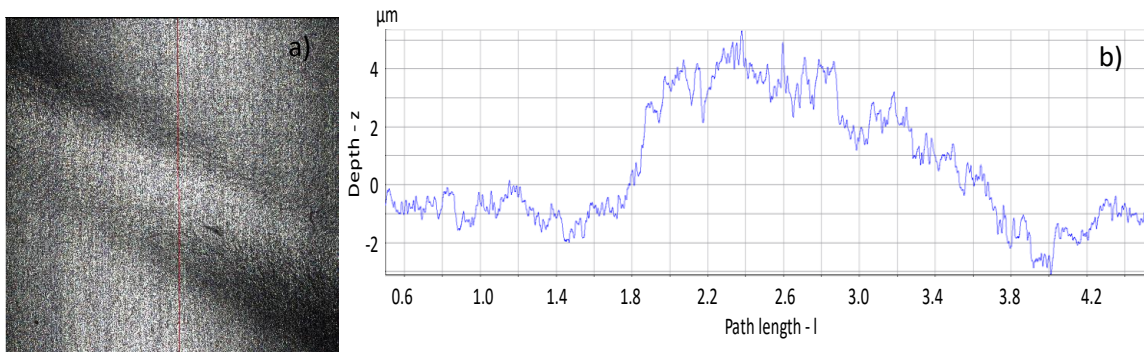
Figure 4.18: a) image of the cold deformed surface with a red line indicating the measurement. b) roughness profile at the red line.

As seen in the Figure 4.18 above, the sampling length extends over the undeformed area of the tube. Although the most of roughness profile is corrected, the filtering does not remove the deformation profile entirely, which results in a hill in the diagram of Figure 4.18b. This hill leads to a significantly overestimated surface roughness. For this reason, the R2D0.4 specimen is excluded from further analysis and conclusions regarding the roughening model. In order to use this specimen or similar thin-deformation profiles, primarily the filtering needs to be adjusted manually. Even with such an adjustment, it is better to use Sa value since Ra averages over a larger distance than the indentation. In Sa, the reported measurement is more local. For more detailed information and illustration on the comparison between Sa and Ra, see appendix C.

With the exclusion of R2D0.4 sample, the slopes of the other curves actually correlate very closely, indicating that the model used is sufficiently accurate for estimating Ra values of indented tubes. At the same time, the model is not equally efficient for thin indentations (even if the roughness filter is improved) since the majority of the measurement length is beyond the cold deformation zone. When it comes to Sa estimation, the model seems to be appropriate for samples cold-deformed with a small radius of curvature. Therefore, evaluation of both Sa and Ra is limited by the geometric parameters of indenter. Nevertheless, the model works reasonably well as a first approximation. Most importantly, this result indicates that the relationship between surface roughness and true strain for biaxially cold-deformed steel tubes is possible to simulate using a linear model.

The model developed by *FS dynamics* in a parallel project was also compared to the experimental data from this study. In those simulations, biaxial strain is calculated, meaning that TD can be evaluated as well. The maximum equivalent plastic strain (PEEQ) of cold deformation with the dimensions of three of the measured specimens was extracted from the model and is tabulated in Table 4.6.

Table 4.6: Maximum PEEQ values derived from FS dynamics simulation model for three different specimens.

Specimen	$PEEQ_{max}$	True $PEEQ_{max}$
R4D1	0.36	0.31
R2D0.4	0.29	0.25
R7D0.8	0.29	0.25

Using the values from the Table 4.6 above together with the surface roughness values from Table 4.3, the true maximum PEEQ for a cold deformation derived from FS dynamics model is plotted against the measured surface roughness values in Figure 4.19.
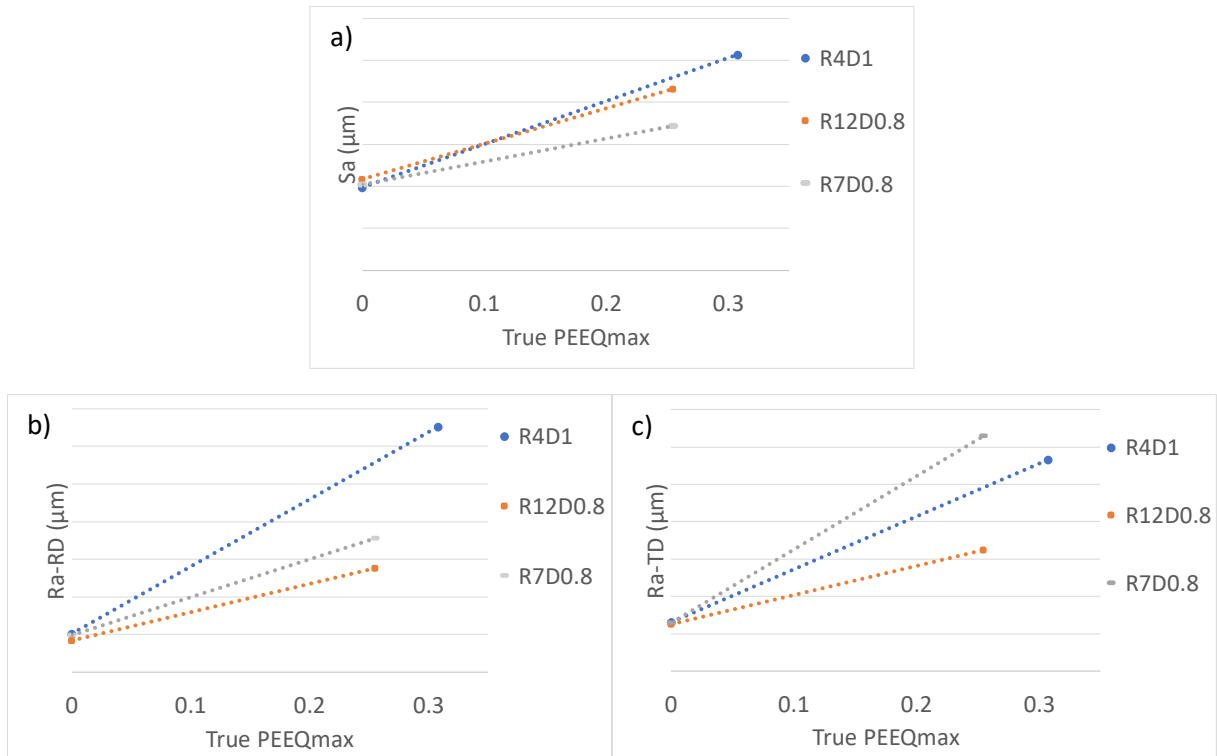
Figure 4.19: Surface roughness plotted against true PEEQ$_{max}$ extracted from the FS dynamic simulation model with linear regressions. a) Sa for the three specimens against true PEEQ$_{max}$. b) Ra measured in roll direction plotted against PEEQ$_{max}$. c) Ra measured in transverse direction plotted against true PEEQ$_{max}$.

The values of the slopes relative to specimen R4D1 is tabulated below in Table 4.7.

Table 4.7: Relative values of slopes of the roughness-true PEEQ$_{max}$ relationship in biaxially strained steel tubes.

Specimen	R4D1	R12D0.8	R7D0.8
Sa	1c	0.82c	0.53c
Ra-RD	1d	0.42d	0.57d
Ra-TD	1e	0.55e	1.39e

From the diagrams in Figure 4.19 and Table 4.7 above, it can be seen that none of the slopes are equal. The lowest and the highest inclinations in each diagram differs with a factor 2-2.5. The strain values were extracted from the single point of a maximum equivalent strain in each indentation, while the surface measurements are conducted over a much larger area or a line. Such a combination is not optimal. This would assume that the strain profiles of different specimens are proportional to each other, which is unlikely. To use this model more accurately, preferably for Sa, the data should be extracted from an area as large as experimental image field of surface roughness measurement. For Ra, the data from a 4 mm long line should be extracted. Such information was not available for extraction when accessing the model, at least during this project. Nevertheless, even if the slopes deviate from each other, they are in the same scale range, which also equals to the scale of slope in the unpolished sheet samples, see Figure 4.10-Figure 4.12 in section *4.2.2 Unpolished sheets*. This is an indication that the model *per se* might still be correct, but the data extraction from the model should be done from an area or a length of the deformation profile.

4.3   Analysis of microstructure evolution

Results of SEM observations in the cross-sectional ND-RD and ND-TD surfaces are shown below. Figure 4.20 below is taken in elemental contrast with BSE detector. It illustrates the microstructure on ND-TD plane.
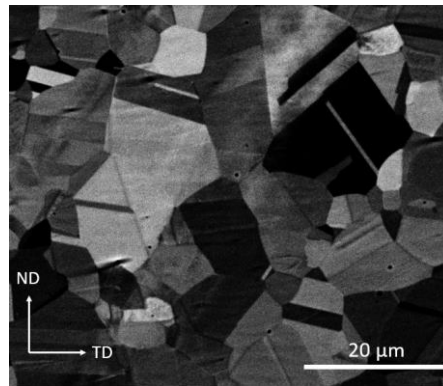
Figure 4.20: SEM image of rectangular ND-TD specimen using BSE detector at 2400x magnification.

A BSE image of cross-section in the RD-ND plane is shown below in Figure 4.21.

Figure 4.21: SEM image of rectangular ND-RD specimen using a BSE detector at 2400x magnification.

From the two figures above, two features can be noted. One is the absence of apparent grain elongations and substructure, indicating that the sheets were fully annealed and recrystallized after the final cold rolling. This is of great importance for modeling both mechanical behavior and the correlation between surface roughness and strain. It indicates that the grain dimension is rather isotropic and thus the effect of microstructure on roughening might be orientation independent. This was not expected before the measurements considering that the optical microscopy on unpolished samples does not allow determination of directions by visual analysis alone. Thus, it implies that the anisotropy of the surface layer is not affected by the bulk crystal structure. The second feature to be noted is the amount of annealing twins. Some grains contain thin straight lines with a contrast in-between different from the rest of the grain. This is due to twinning within the grain. Since the grains seem to be fully annealed, these are annealing twins. The two figures do give qualitative information. EBSD measurements resulted in more quantitative information.

Result from one of the EBSD scans performed on the polished TD specimen 1 is shown in Figure 4.22.
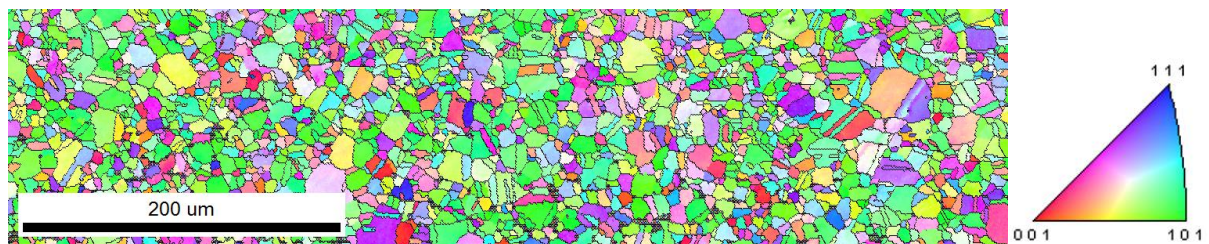
Figure 4.22: Inverse pole figure map of polished TD specimen 1. Color code for crystal orientation with scale shown on the right-hand side.

From the Figure 4.22, many twins can be seen within the grains. For the average intercept length of the grains, twinning was excluded from the analysis, and the resulting grain map is shown below in Figure 4.23
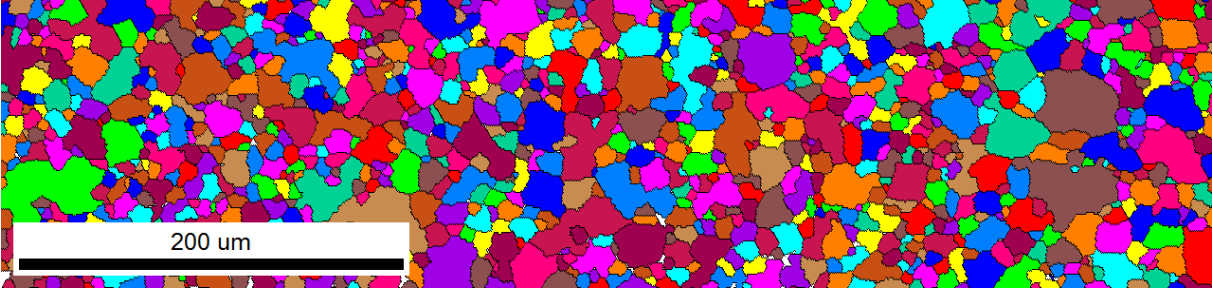
Figure 4.23: Grain map of polished TD specimen 1. The color code is random just to separate the grains visually.

Twinning was excluded from calculations in all the scans, and the average grain boundary intercept length was calculated for both RD and TD. Respective values are summarized in Table 4.8 and the grain size distributions of a representative scan is shown in Figure 4.24.

Table 4.8: Average grain boundary intercept length in RD and TD

Direction	Intercept length (µm)	SD (µm)
RD	6.68	0.14
TD	8.63	0.21
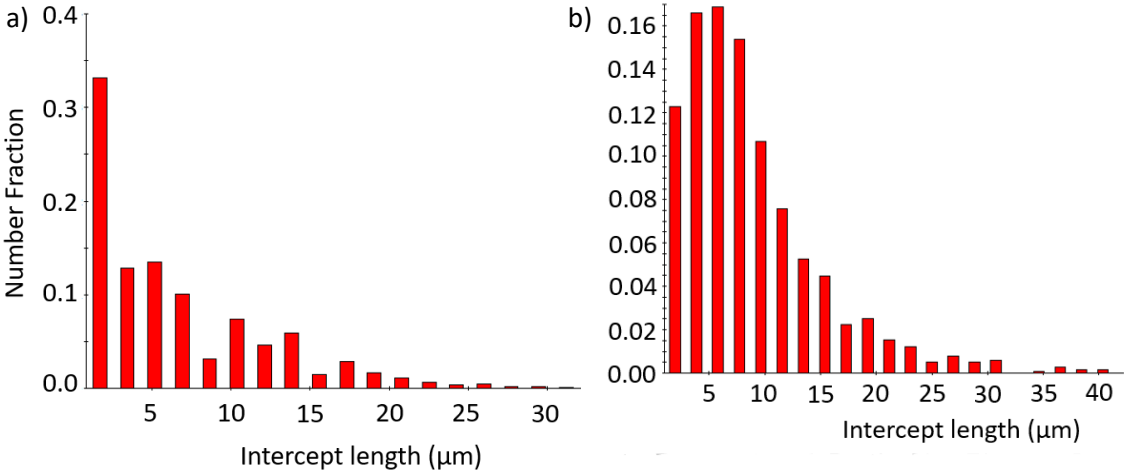
Figure 4.24: Distribution of intercept lengths for grain boundaries in a) RD and b) TD.

From the grain boundary intercept data extracted from EBSD, it is evident that the grains are noticeably longer in TD than in RD. The ratio between TD and RD equals to 1.29. The aspect ratio of the grains was measured to be 0.44 on average with SD=0.01. This results in a ratio of 1.27. Since both of the separate measurements resulted in such close values, it is a strong indication of adequate data processing. The main reason of larger grain sizes in TD than in RD is the build-up of dislocations and stresses during rolling. As mentioned, typical rolling microstructure shows grains longer in RD than in TD since grains are strained in RD more than in TD. When annealing is conducted, it might happen that recrystallization in RD needs less energy than that in TD due to differences in the amount of residual stresses leading to recovery only in TD but at least certain degree of recrystallization in RD.

For the equation (6), derived by Osakada and Oyane in [6], it was stated that roughening rate was proportional to the grain size. From the linear regressions of the relationship between Sa and Ra and

true strain for the unpolished samples (see Figure 4.10 and Figure 4.11), the ratio between the slopes of the curves is α_{TD} : α_{RD}=1.12 for both Sa and Ra. The ratio between grain dimensions of 1.28 is larger than the one of roughness rate by approximately 14 %. For the material used in this master's thesis, these ratios do not directly correlate the linear relationships between grain size and roughening rate. The constant, k, correlating the grain size and the roughening rate was experimentally determined as 0.5 for FCC material according to Osakada and Oyane [6]. For the 316L samples in this study, k approximately is 4-5. Even though this result does not agree with their study, the roughening rate is still larger in the direction with the largest grain dimension, and therefore can be correlated. For the polished specimens, by comparing the roughening rates at the low strain levels and approximate this to be linear, the ratio between roughening rate of TD and RD is α_{TD}:α_{RD} is 1.50:1 for Sa. This results in an even larger ratio and differs even more from the grain dimension ratio. Still, the relationship between large grain dimension and large roughening rate holds.

To investigate further the case of anisotropy of the material, the texture of the polished TD specimen 1 was extracted from the EBSD data. In Figure 4.25 below, a (111) texture plot is shown. This illustrates how the (111) planes are oriented relative to RD and TD of the specimen.
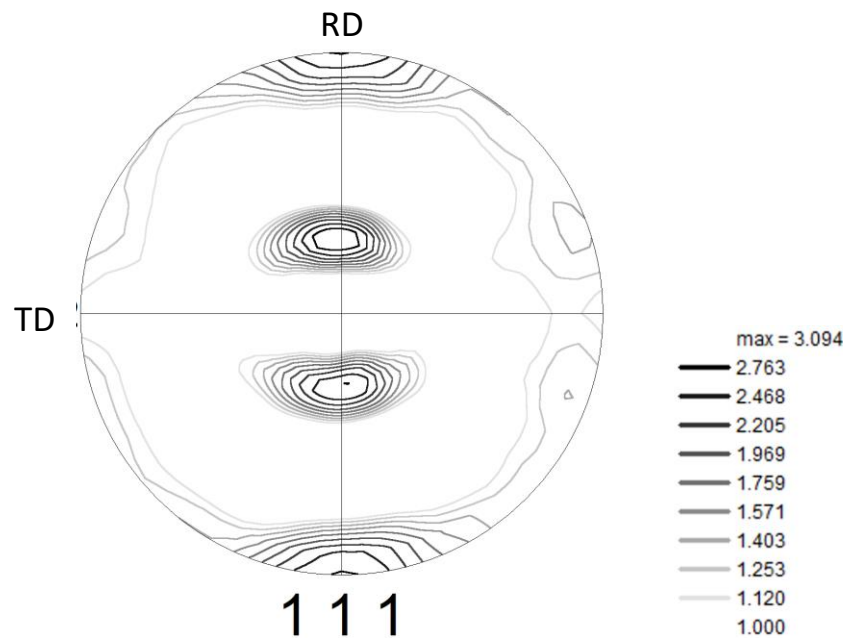
Figure 4.25: (111) pole figure illustrating texture in the as-received SS316L steel samples.

From the Figure 4.25 it is seen that the material has a weak texture. The scale bar is normalized by the intensity of randomly distributed grain orientations. A maximum of 3.094 thus mean that the most represented orientation is approximately three times as common as the least represented orientations. The two strongest orientations are the ones with the (111) normal parallel to RD and at approximately 58° inclined away from RD towards ND. This texture is typical for annealed 316L steel [27, 28]. It has been found that for 316L, the cold rolled texture is similar to the annealed one, but from both SEM images and EBSD analysis above, it is concluded that the texture is of annealing type.

When tensile load is applied to a homogeneous body, the maximum shear force is inclined at 45° to the tensile axis and the minima (zero shear stress) are in the directions parallel and orthogonal to the tensile axis. Since the primary slip system in FCC metal is within the (111) plane, the preferred orientation of grains with the (111) normal parallel to RD will have no shear stress within the slip plane when the tensile axis is in RD or TD. However, when the tensile axis is in 45°, the resolved shear stress

is at its maximum in this plane. To determine the resolved shear stress of the slip system, slip directions need to be known as well, which can be used to obtain further information of what effect the texture has. Such analysis is outside of the scope of this thesis but could be useful in future studies.

For the martensite analysis of unstrained steel sheets, the average fractions of different phases in unstrained specimens is summarized in Table 4.9 from four measurement areas of 630x150 μm^2 each.

Table 4.9: Phase composition of unstrained specimen

Phase	Average (%)	SD (%)
Austenite	99.43	0.2073
Martensite	0.3894	0.1389
Ferrite	0.185	0.0706

As seen from the Table 4.9, the majority of microstructure in the material used is austenitic phase with very small traces of martensite and ferrite. The martensite level of the specimen, when strained to 0.3 engineering strain was measured to be 0.402 %, which was considered to be negligibly small in the context of this work. The data indicate that the initial martensite level is too low to have any impact and neither does the martensite level increase while deforming the material.

4.3.1 Polished sheets

To evaluate the hypothesis of grain rotation, SEM images were taken of a polished specimen before and after exposure to an engineering strain of 0.30. The images were taken using SE and BSE detectors with topological and compositional contrast measurements, respectively. These are shown in in Figure 4.26.
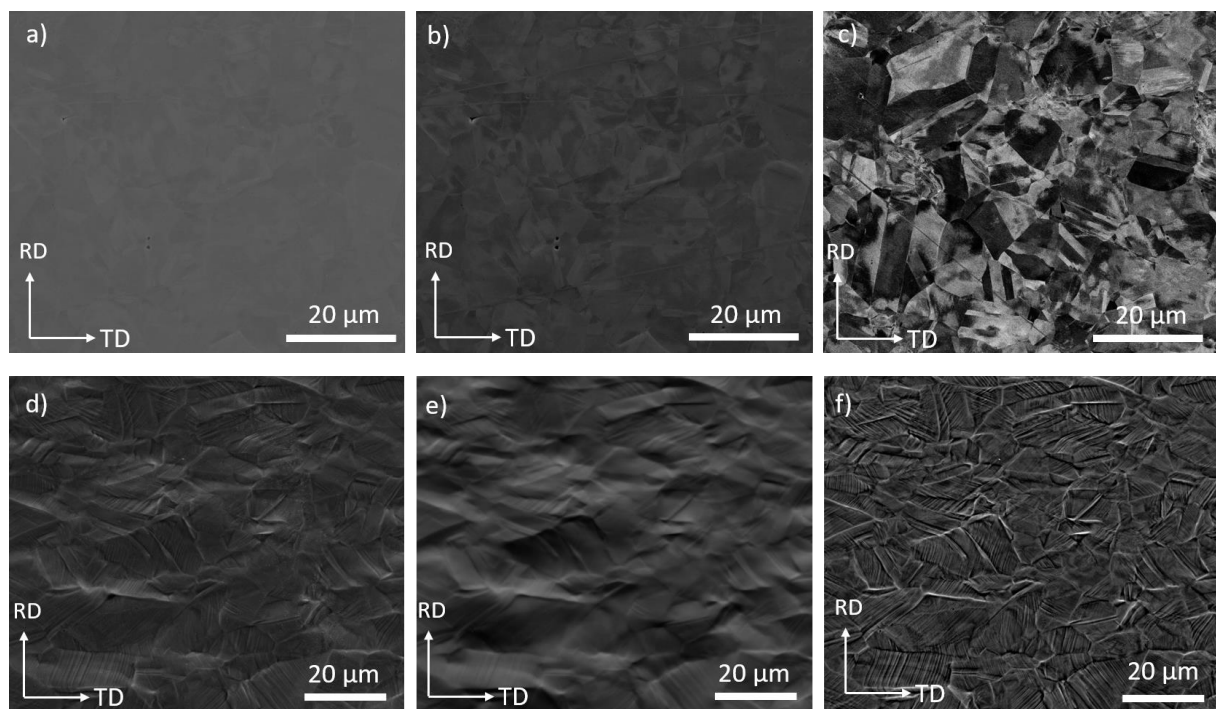
Figure 4.26: SEM images of a specimen before, a), b) and c), and after, d), e), and f), exposure to an engineering strain of 0.30 in TD. images are taken with SE detector a), d), BSE detector using topological contrast, b), e), and BSE detector with compositional contrast, c), f).

When unstrained, the specimen gives virtually no contrast in the SE detector, Figure 4.26a. From the BSE images grain structure can be observed. Low-contrast is obtained in topological mode, Figure 4.26b, vs high-contrast in compositional or elemental mode, Figure 4.26c. The contrast acquired from

the BSE detector in topological mode is not topological only, also having some elemental component, as can be judged from the appearance of the image. This is not unusual for smooth surfaces, since topological mode is not able to completely exclude all of the elemental contrast. From the image taken with the SE detector in the deformed specimen, several surface characteristics can be seen, Figure 4.26d. The SE detector primarily picks up edge and topography contrast, but also some elemental contrast. The surface is seen to be relatively rough and contains segments of striped areas. For the two images, Figure 4.26e and f taken with the BSE detector, Figure 4.26e is sensitive to topological properties while Figure 4.26f to composition. In Figure 4.26f, the bright contrast shows grain boundaries and the light-grey parallel stripes within grains are slip bands produced by dislocation slip in the grains. It can also be seen that the majority of contrast in Figure 4.26e correlates with that of the grain boundaries in Figure 4.26f. There is some contrast in the slip planes as well, but not at all to the same extent. This indicates that the grain boundaries generate the majority of surface roughness, which supports the hypothesis of grain rotation.

As a complementary measurement, 3D optical microscopy at high magnification using polarized light shows slip bands and topographic structures at grain boundaries as well, as illustrated by the images in Figure 4.27 below.
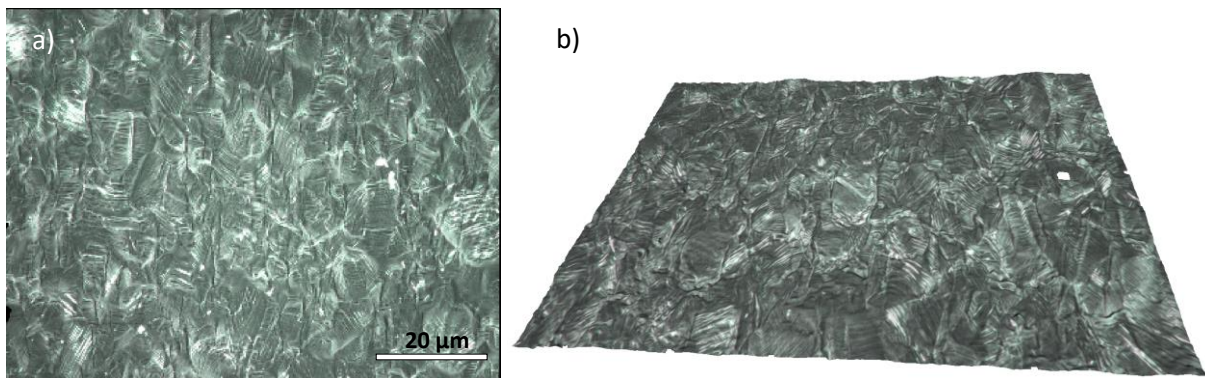
Figure 4.27: 3D FV-microscope image taken with polarized light. The left image emphasizes the slip bands, and size of the surface characteristics, a). The right image emphasizes topographic structures, b).

In both of the figures Figure 4.26 and Figure 4.27, qualitative information on the size of the roughness wavelength is obtained. To determine this quantitively, the roughness profile of a 4 mm scan of RD polished specimen 4 is analyzed. The roughness profile together with the peak-to-peak distance distribution of the roughness profile is shown in Figure 4.28.
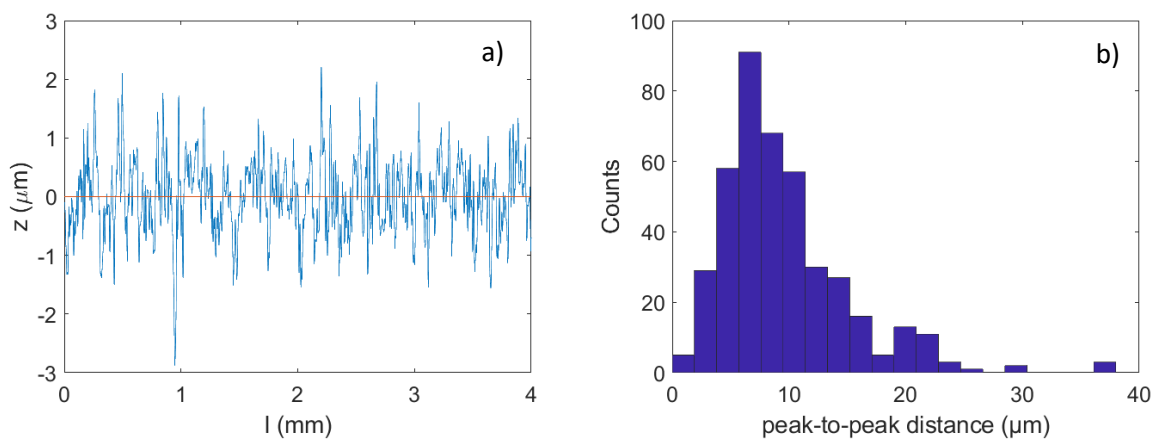
Figure 4.28: Roughness profile (a) and peat-to-peak distribution (b) of RD polished specimen 4.

From the Figure 4.28, it is seen that the distances between peaks are of the same magnitude as the size of grains. The average peak-to-peak distance of the roughness profile is 9.5 µm, compared to the average grain boundary intercept length of RD being 6.7 µm. The grain size is somewhat smaller, but this was expected since not all grain boundaries necessarily result in a peak. The waves of the roughness profile are in the same order as the grain boundary intercept length, which indicates that the roughness is primarily affected by grains which again strengthens the hypothesis of grain rotation.

4.3.2 Unpolished sheets

To understand why the behavior of surface in the polished and unpolished specimens differ so much the surface of the unpolished sheets was imaged using SEM, as illustrated in Figure 4.29 below.
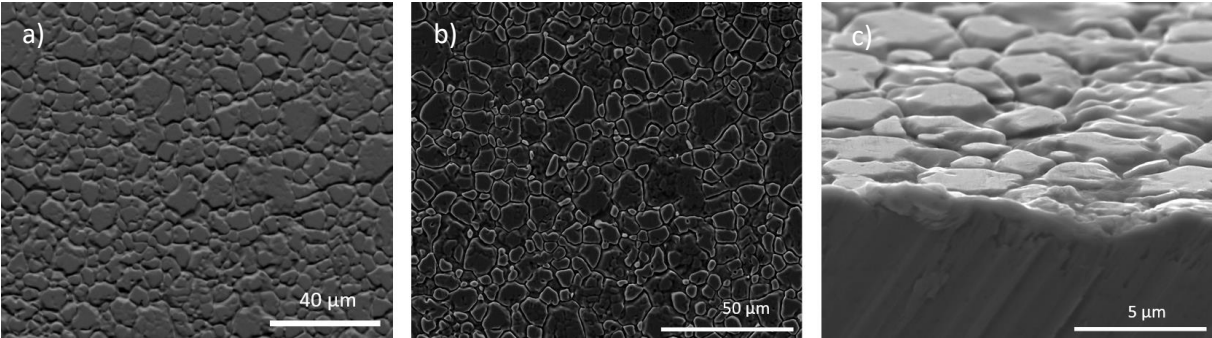
Figure 4.29: SEM images of unpolished specimen. a) image taken with topological BSE detector. b) image of surface taken in SE detector mode. c) high magnification SE image of tilted specimen showing the cross-section of a cut surface (lower half) and the top surface (upper half).

From the images above, a scale-like structure is observed on the surface. The scales are in the same order of size as the grains and were from SEM imaging evaluated to be 1 µm thick. To evaluate if it is a passivation layer, EDS measurement was performed on a polished and an unpolished specimen. The average oxygen count from five measurements of each specimen is shown below in Table 4.10

Table 4.10: Results from EDS measurements on unpolished and polished sheet.

Area	Average oxygen count	SD
Polished	154	29
Unpolished	324	35

From the result it is evident that the scalar layer on top of the unpolished steel sheet is an oxide layer. This explains why the behavior differ between polished and unpolished surfaces. The oxygen layer is more brittle than the ductile steel below it. Therefore, it behaves differently when exposed to strain. It is however thin compared to the grain size. Therefore, it is most likely affected by the austenitic steel grains underneath. SEM images from an unpolished specimen strained to ε=0.30 in transverse direction is shown in Figure 4.30.
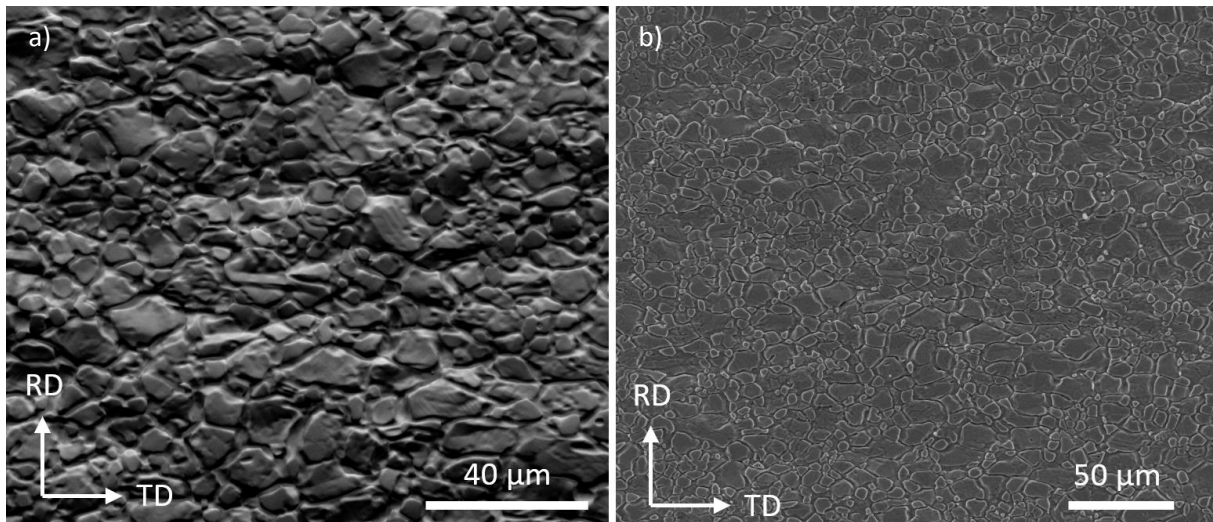
Figure 4.30: SEM images of TD specimen strained to ε=0.30 taken with topological BSE detector (a) and SE detector (b).

From the images above, a clear difference between the surface is seen compared to the unstrained specimen of Figure 4.29. From BSE image, Figure 4.30a, two surface profile characteristics are seen: (i) large waves extending over several scales and (ii) boundaries between individual scales. The latter also seem to be rougher for the strained specimen. Therefore, two roughening processes seem to be occurring when deforming unpolished 316L sheets and tubes. It is possible that the roughening generated at the grain boundaries is caused by grain rotation occurring in the austenitic grains underneath the surface, while the larger waves are generated by the brittleness of the oxide layer, which is not able to deform compatibly with the macroscopic deformation of the substrate steel due to a lack of ductility.

To evaluate the wave components of unstrained specimens, a roughness profile from a 4 mm scan in the unpolished specimen strained to a 30 percent elongation in RD was analyzed. Figure 4.31 below show the roughness profile of a section of the measurement.
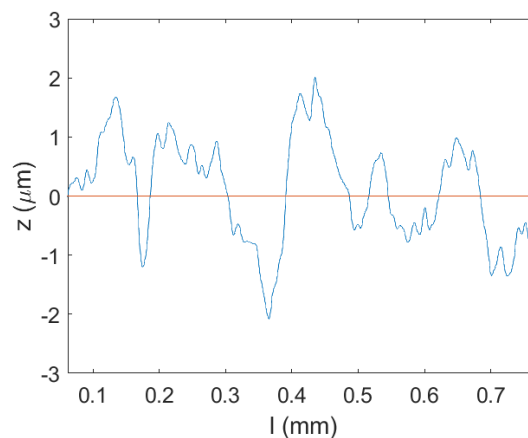
Figure 4.31: Roughness profile of specimen strained to an engineering strain of 0.30. The y-axis shows the depth in microns and the x-axis the measurement distance in mm.

From the Figure 4.31 above, the roughness profile seems to consist of two wave components. One with a large amplitude that is oscillating across the y-axis, and one with fine oscillating component which contains a smaller amplitude and a higher frequency. Two methods have been used for separating these two components. In the one presented first, the distribution of distances between y-axis intersects is compared to the distribution of distances between peaks. The intersect distances

would represent the roughness generated by the longwave component and the peak-to-peak distances represent the shortwave component, which would be of the same scale as the oxide and grains.
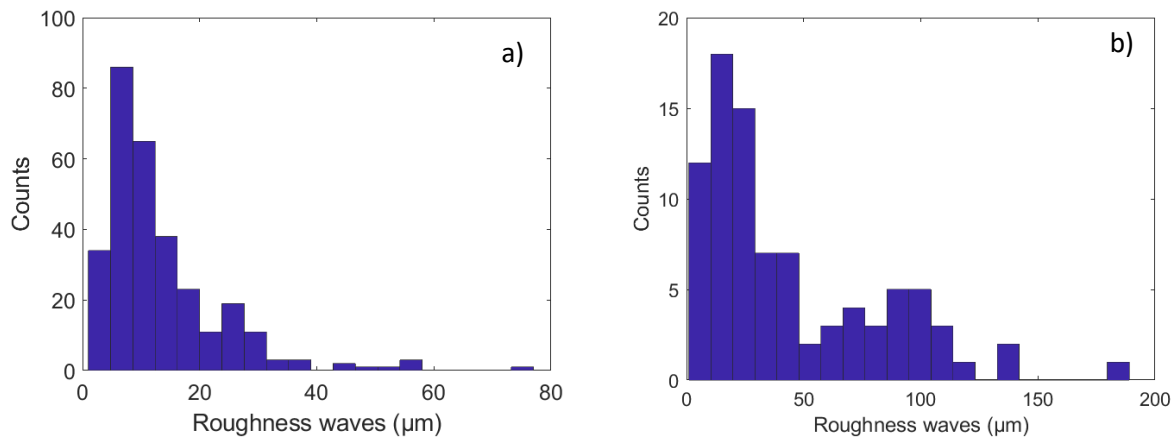
Figure 4.32: Histogram showing the distribution of peak-to-peak distance (a) and zero depth intersection distance (b).

In the diagram of Figure 4.32a above, the major distribution is seen to be at a magnitude lower than 30-35 µm. The largest bin is centered at 6.7 µm and the average distance is 13.3 µm. The average grain intercept length in RD was measured to be 6.68 µm which correlates very well with the maximum frequency. It is also in the same order of magnitude as the average peak distance. This indicates that the peaks generate at the grain boundaries (or scale boundaries). In the diagram of Figure 4.32b, two different regions are distinguishable. One below 50 microns and one between 50 and 125 microns. From a visual inspection of the roughness profile, it was seen that at some regions the depth of the surface was at an amplitude enabling the fine oscillating component to oscillate across the y-axis. This results in the fine oscillation also contributing to the distribution. The two different regions seen in the right diagram is therefore considered to be the two different wave components.

The other method for separating the wave components was fast Foriertransform (FFT) on the roughness profile data. The result from this is seen in the diagram Figure 4.33. To remove low- and high frequency noise the x-limits was set as (0.0065, 0.05).
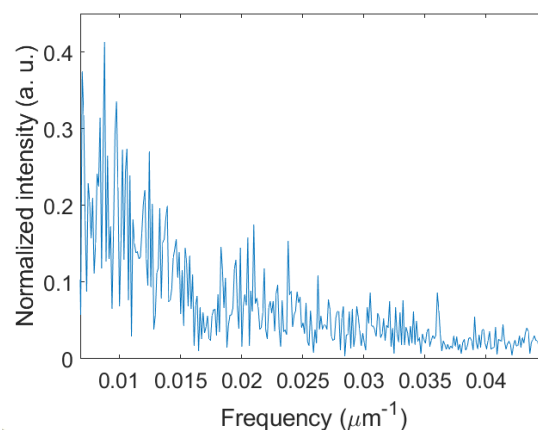
Figure 4.33: Diagram of FFT performed on roughness profile extracted from roughness measurements of RD unpolished specimen strained to ε=0.30. Intensity on y-axis and frequency (one over distance) on x-axis.

The FFT data presented in the diagram is found to contain a dip at approximately 0.017 µm^{-1} which equals 59 µm in the real-space domain. On the left side of this dip there is a hill-like region, extending

to a measured minimum of 0.0068 μm^{-1}, which equals 147 μm. The size region of this domain is similar to the long wave distribution region in Figure 4.32. It thus indicates that there is a longwave roughness component in an approximate size region of 60-130 μm, which equals to 10-20 grains. To the right of the dip in the figure above, the high-frequency domain is extending quite far, and it was not possible to tell where the FFT start showing noise instead of relevant data.

Conclusions

The scope of this thesis was to obtain knowledge of strain-induced surface roughness on 316L austenitic stainless steel, by determining the mechanism responsible for surface roughening and to find the correlation between strain and surface roughness.

For polished 316L steel sheet, surface roughness increases with engineering strain up to 0.15, then decreases about 25% to a level where roughness no longer is affected by changes in strain levels. This roughness is localized at the grain boundaries and attributed to grain rotation due to shear in a primary slip system as the surface roughness increases. The decrease in surface roughness is attributed to grain subdivision, and grain rotation arising from dislocation glide in secondary slip systems. The distance between adjacent peaks in the roughness profile appears to be lognormal.

SEM and EDX studies confirmed that unpolished 316L contained a 1 μm thick oxide layer with a scale like structure, with a morphology and size similar to that of the austenitic grains of the bulk material. The dependence of surface roughness on strain can be considered linear over the entire strain interval measured. The roughness profile of the oxide surface appears more complex with two different wave components. The shortwave component is derived from underlying grain rotation, and the longwave component can be attributed to the separation of oxide layer form the base metal due to lack of ductility. The slope coefficient in the Sa-e diagram was orientation dependent (RD, TD, 45º) with $\alpha_{RD}=1.32$, $\alpha_{TD}=1.47$ and $\alpha_{45º}=1.44$. From the Ra-e diagram, the coefficients were extracted as $\alpha_{RD}=1.68$, $\alpha_{TD}=1.89$ and $\alpha_{45º}=1.61$.

EBSD analysis of both austenitic grain structure and texture revealed substantial anisotropy in the as-supplied material. The ratio between the average grain boundary intercept in RD and TD was 1:1.29. This is about 14% lower than the ratio between the slope coefficients. No linear relationship between grain size and roughness rate was thereby detected, but there seems to be a correlation between the two. Texture analysis showed a weak annealing texture in unstrained 316L, with the [111] direction parallel to the RD and inclined 70° from the RD towards ND.

The relationship between surface roughness and true strain for the tubular 316L could be approximated as linear for both uniaxial and biaxial strains. Of the two models for predicting the roughness of steel tubes caused by a biaxial strain process, the model based on a 1D calculation of true strain in the rolling direction showed a relatively good fit for Ra-values with some constraints on the indentation size. The other model based on $PEEQ_{max}$ values obtained from a simulation done by *FS dynamics*, was not as good at roughness prediction. Also, it did not make use of the full potential of the simulation. Based on how it related to uniaxially strained specimens, it is suggested that for an accurate model, the simulation by FS dynamics is to be used. Yet, instead of extracting a single value of $PEEQ_{max}$, a strain profile is required.

Future work

From the literature survey it was found that the strain rate has a great effect on the surface roughening, by that a high strain rate lowers the surface roughening. In studies of surface asperity flattening, which is the phenomena of a decreased surface roughness on the contact side upon deforming a material it was noted that an increased strain rate led to a more reduced surface roughness. In this master's thesis the free surface was studied on which the roughness increases with strain, so it is not the same effect investigated. However, what was found interesting in the studies was their discussion on why the rate of surface roughness reduction increased with increasing strain rate, which was due to that when the strain rate increased more slip systems were involved, leading to a lower roughness [29, 30].

The strain rate of one of the biaxially strained specimens, R4D1, was calculated to be 13.7 s^{-1} with the calculation seen in appendix D. To evaluate what effect an increase in strain rate has on the material, the flow stress is investigated. The flow stress is dependent of the strain rate according to the Johnson-Cook material model as shown below in equation (8) [31].

$$\sigma = (A + B\epsilon^n)(1 + Cln\dot{\epsilon}^*)(1 - T^{*m}) \qquad (8)$$

This equation was developed by Gordon R. Johnson and William H. Cook as a model for von Mises tensile flow stress, σ. ϵ is the equivalent plastic strain, $\dot{\epsilon}^* = \dot{\epsilon}_p/\dot{\epsilon}_0$ is the dimensionless plastic strain rate where $\dot{\epsilon}_p$ is the plastic strain rate and $\dot{\epsilon}_0 = 1.0$ s^{-1} is the reference plastic strain rate. T^* is the homologous temperature and A, B, n, C, m are material constants [32]. From the equation it is seen that the strain rate dependent factor is $(1+Cln\dot{\epsilon}^*)$. From a review article on empirically determines of the C parameter for 316L stainless steel, the parameter has been determined to be between 0.01-0.1 with an average 0f 0.0598 [33]. Applying the average value of C, by increasing the deformation rate/strain rate with a factor of two, the flow stress would increase with 16 %.

It is also needed to investigate the weld. From a few roughness measurements conducted on the weld line (data not presented) it was evident that it differed from the rest of the specimens. Not enough data was collected for any analysis to be conducted but it was obvious that it is an area that need to be looked in to. The welding is thought to have a great effect on the microstructure of the material regarding the size and shape of the grains. Li Lichan et. al [34] conducted a study on how grain size and material phase Is affected by welding at different distances from the weld zone of a 316L stainless steel. Their conclusions were that in the fusion zone the grains became larger than their primary state and that the phases in the fusion zone are austenite and ferrite dual-phase. They also investigated four areas close to the welding (heat affected zones, HAZ's, 1-4) and noticed that the grain size between the different fusion zones varied. From the study it is clearly illustrated that both phase composition and grain size is affected by welding. A proposal is that a similar type of experiment conducted on the tubular sections is to be repeated with the sections measured containing a weld line.

Lastly, to develop further knowledge and understanding of strain-induced surface roughening of 316L steel and to be able to better predict the roughness of cold deformed steel tubes one need to look further into texture development of 316L during strain. By measuring the roughness and perform EBSD scans of the same area for several strain levels, one would be able to follow the process of individual grains for different strains. By looking into the Schmidt factor, it should also be possible to determine which grains are exposed to the most resolved shear stress in the slip planes and measure how rotation of these occur. This type of experiment would give very accurate information on the exact mechanism and could be used for precise predictions of surface roughness.

References

1. Smallman, R.E. and A.H.W. Ngan, *Modern physical metallurgy*. eight ed. 2014: Elsevier Ltd.
2. Turkoz, E. *Princeton*. 2016; Available from: https://www.princeton.edu/~eturkoz/materials.html.
3. Institution, S.S., *SS-EN_ISO_4287*, in *Geometriska produktspecifikationer (GPS) – Ytstruktur: Profilmetod – Termer, definitioner och parametrar för ytstruktur*. 1998.
4. solutions, T.s., *Aerospace Engineering Guide.* 2008.
5. Stoudt, M. and J. Hubbard, *Analysis of deformation-induced surface morphologies in steel sheet.* Acta Materialia, 2005. **53**(16): p. 4293-4304.
6. Osakada, K. and M. Oyane, *On the Roughening of Free Surface in Deformation Process.* Bulletin of JSME, 1971. **29**(258): p. 171-177.
7. Stoudt, M.R., et al., *A Study of the Fundamental Relationships between Deformation-Induced Surface Roughness and Strain Localization in AA5754.* Metallurgical and Materials Transactions A, 2009. **40**(7): p. 1611-1622.
8. Dautzenberg, J.H. and J.A.G. Kals, *Surface Roughness Caused by Metal Forming.* CIRP Annals, 1985. **34**(1): p. 477-479.
9. Guangnan, C., et al., *Roughening of the free surface of metallic sheets during stretch forming.* Mateerials science and engineering A, 1990. **128**: p. 33-38.
10. Romanova, V.A., et al., *Micromechanical model of deformation-induced surface roughening in polycrystalline materials.* Physical Mesomechanics, 2017. **20**(3): p. 324-333.
11. Stoudt, M.R., et al., *Effect of uniaxial strain on the surface roughness.* Magnesium Technology, 2004: p. 269-274.
12. Zhou, X.H. and X. Su, *Effects of deformation mode on surface roughening of austenitic stainless steels.* Materials Science and Technology, 2013. **27**(6): p. 1040-1044.
13. Stoudt, M.R., J.B. Hubbard, and S.D. Leigh, *On the Relationship Between Deformation-Induced Surface Roughness and Plastic Strain in AA5052—Is it Really Linear?* Metallurgical and Materials Transactions A, 2011. **42**(9): p. 2668-2679.
14. Solomon, N. and I. Solomon, *Deformation induced martensite in AISI 316 stainless steel.* Revista de Metalurgia, 2010. **46**(2): p. 121-128.
15. Abreua, H.F.G.d., et al., *Deformation Induced Martensite in an AISI 301LN Stainless Steel-Characterizatin and Influence on Pitting Corrosion Resistance.* Materials Research, 2007. **10**(4): p. 359-366.
16. Sanusi, K.O. and K.O. Hussein, *Investigation of corrosion effect of mild steel on orange juice.* African Journal of Biotechnology, 2011. **10**(16): p. 3152-3156.
17. Khadom, A.A., et al., *The Effect of Temperature and Acid Concentration on Corrosion of Low Carbon Steel in Hydrocloric Acid Media.* American Journal of Applied Sciences, 2009. **6**(7): p. 1403-1409.
18. Yaro, A.S. and R.K.W.A.A. Khadom, *REACTION KINETICS OF CORROSION OF MILD STEEL IN PHOSPHORIC ACID.* Journal of the University of Chemical Technology and Meallurgy, 2010. **45**(4): p. 443-448.
19. Danzl, R., F. Helmli, and S. Scherer, *Focus Variation – a Robust Technology for High Resolution Optical 3D Surface Metrology.* Strojniški vestnik – Journal of Mechanical Engineering, 2011. **2011**(03): p. 245-256.
20. Adams, A.J.S.M.K.B.L. and D.P. Field, *Electron Backscatter Diffraction in Materials Science*. 2nd ed. 2009: Springer.
21. Suwas, S. and R.K. Ray, *Representation of Texture*, in *Crystallographic Texture of Materials*. 2014. p. 11-38.
22. Weidner, A., et al., *Texture evolution of cold rolled and reversion annealed metastable austenitic CrMnNi steels.* IOP Conference Series: Materials Science and Engineering, 2015. **82**.
23. Fang, Z., et al., *Electron-momentum spectroscopy of crystal silicon.* Physical Review B, 1998. **57**(20): p. 12882-12889.

24. Corporation, A.S., *316/316L Stainless Steel.* 2016.
25. ASTM, *Designation: E8/E(M-16a Standard test Methods for Tension Testing of Metallic Materials.* ASTM internatnional, 2016.
26. Institution, S.S., *SS-EN_ISO_6892-1*, in *Metallic materials – Tensile testing – Part 1: Method of test at room temperature*. 2016.
27. De Cooman, B.C., Y. Estrin, and S.K. Kim, *Twinning-induced plasticity (TWIP) steels.* Acta Materialia, 2018. **142**: p. 283-362.
28. DONADILLE, C., et al., *Development of texture and microstructure during cold-rolling and annealring of F.C.C alloys example of an austenitic stainless steel.* Acta metall, 1989. **37**(6): p. 1547-1571.
29. Jiang, Z. and H. Xie, *Application of Finite Element Analysis in Multiscale Metal Forming Process*, in *Finite Element Method - Simulation, Numerical Analysis and Solution Techniques*. 2018.
30. Li, H., *A study of surface roughness in the metal forming process*, in *Faculty of engineering*. 2012, University of Wollongong.
31. Skrinjar, O., *High Speed Tensile Testing of UHSS Material*. 2009: Swerea KIMAB AB.
32. Cook, G.R.J.W.H., *Fracture characteristics of three metals subjected to various strains, strain rates, temperatures and pressures.* Elsevier, 1985.
33. Umbrello, D., R. M'Saoubi, and J.C. Outeiro, *The influence of Johnson–Cook material constants on finite element simulation of machining of AISI 316L steel.* International Journal of Machine Tools and Manufacture, 2007. **47**(3-4): p. 462-470.
34. LiChan, L., et al., *Effect of Welding Heat Input on Grain Size and Microstructure of 316L Stainless Steel Welded Joint.* Applied Mechanics and Materials, 2013. **331**: p. 578-582.

Appendices

A. Evaluation of Specimen dimensions

The specimen dimensions of the dog-bone sheet specimens are tabulated in Table A.1 below.

Table A.1: Table of specimen dimensions

Dimension	Size (mm)
Thickness, T	0.8
Width, W	4.2
Gauge length, G	21
Radius of fillet, R	3.49
Sample length, L	45.5
Parallel length, A	23.625
Grip length, B	7.5
Grip width, C	10

To determine appropriate dimensions of the samples ISO standards and ASTM standards were investigated. Two criteria that were set for our specimens were, a) the width should be less than 9.4 mm to overcome the ultimate tensile strength of the material. This criterion derives from that the maximum capacity of the Instron Electropulse E10000 is 7.5 kN and that if the materials has been work hardened it is needed to reach stress levels of approximately 1000 MPa to fracture (see Figure 3.1). b) the maximum overall length is approximately 45 mm due to that the material from which specimens are cut out is 49.7 mm in width and a few mm is needed as a margin for the water jet cutting.

From a comparison it was concluded that the ASTM standards was best suited for the specimens. The ASTM standards had three different standard specimens for tensile testing of metal sheets with a thickness between 0.13 mm and 5.0 mm, the table is seen below in Figure A.1.

	Dimensions		
	Standard Specimens		Subsize Specimen
	Plate-Type, 40 mm [1.500 in.] Wide	Sheet-Type, 12.5 mm [0.500 in.] Wide	6 mm [0.250 in.] Wide
	mm [in.]	mm [in.]	mm [in.]
G—Gauge length (Note 1 and Note 2)	200.0 ± 0.2 [8.00 ± 0.01]	50.0 ± 0.1 [2.000 ± 0.005]	25.0 ± 0.1 [1.000 ± 0.003]
W—Width (Note 3 and Note 4)	40.0 ± 2.0 [1.500 ± 0.125, -0.250]	12.5 ± 0.2 [0.500 ± 0.010]	6.0 ± 0.1 [0.250 ± 0.005]
T—Thickness (Note 5)		thickness of material	
R—Radius of fillet, min (Note 6)	25 [1]	12.5 [0.500]	6 [0.250]
L—Overall length, min (Note 2, Note 7, and Note 8)	450 [18]	200 [8]	100 [4]
A—Length of reduced parallel section, min	225 [9]	57 [2.25]	32 [1.25]
B—Length of grip section, min (Note 9)	75 [3]	50 [2]	30 [1.25]
C—Width of grip section, approximate (Note 4 and Note 9)	50 [2]	20 [0.750]	10 [0.375]

Figure A.1: Figure of table over specimen dimensions suggested by the ASTM standards. Taken from [25].

The only sample to fulfill criterion a) is the sub size sample with a width of 6.0 mm. However, just as for all the three specimen dimensions it violates criteria c). It is thus needed to scale down the dimensions. Since there were uncertainties of how far from the edges that the water jet cutter would affect the specimen. A wide gauge length was therefore preferred, and it was decided to use the standard specimen dimensions with a width of 40 mm and scale this down by a factor of 10. The grip width was widened some but the important relationship between gauge width and gauge length remained.

B. Surface roughness data

Table B.1: Table listing surface roughness parameters for polished samples strained in RD at strain levels between zero strain to breakage.

Strain	0	0.0489	0.15	0.2254	0.326	0.449
Sa	0.163	0.4192	0.583	0.5308	0.4856	0.478
Ra		0.393333	0.575167	0.547667	0.501333	0.492833

Table B.2: Table listing surface roughness parameters for polished samples strained in TD at strain levels between zero strain to breakage.

Strain	0	0.0478	0.15	0.2255	0.3	0.4504
Sa	0.163	0.537667	0.745167	0.585833	0.5665	0.468833
Ra		0.543333	0.7375	0.571167	0.583667	0.505333

Table B.3: Table listing surface roughness parameters for polished samples strained in 45° at strain levels between zero strain to breakage.

Strain	0	0.0482	0.15	0.2254	0.343	0.4209
Sa	0.163	0.4805	0.662667	0.587333	0.523667	0.566167
Ra		0.472333	0.674833	0.582667	0.515667	0.570167

Table B.4: Table listing surface roughness parameters for unpolished samples strained in RD at strain levels between zero strain to breakage.

Strain	0	0.143	0.305	0.447	0.558	0
Sa	0.1281	0.3482	0.5135	0.6142	0.6426	0.1281
Ra	0.1271	0.439167	0.6425	0.7498	0.905667	0.1271

Table B.5: Table listing surface roughness parameters for unpolished samples strained in TD at strain levels between zero strain to breakage.

Strain	0	0.143	0.309	0.452	0.58	0
Sa	0.1281	0.376	0.561833	0.678	0.712667	0.1281
Ra	0.1271	0.449167	0.710833	0.82275	0.845833	0.1271

Table B.6: Table listing surface roughness parameters for unpolished samples strained in 45° at strain levels between zero strain to breakage.

Strain	0	0.151	0.313	0.451	0.592	0
Sa	0.1281	0.348	0.542833	0.6595	0.6585	0.1281
Ra	0.1271	0.3975	0.612	0.720833	0.769333	0.1271

Table B.7: Table listing surface roughness parameters for tubular sections at strain levels between zero strain to fracture.

Strain	0	0.151	0.300	0.450	0.635	0
Sa	0.3489	0.6668	0.982	1.1935	1.236	0.1281
Ra	0.3483	1.047	1.500	1.770	1.680	0.1271

C. Sa compared to Ra

To illustrate the difference in surface roughness depending on the location of measurement, Sa has been measured for several locations covered by the Ra measurement over the cold deformed part of specimen R2D0.4. The measurement areas are illustrated by red squares Figure C.1 below.
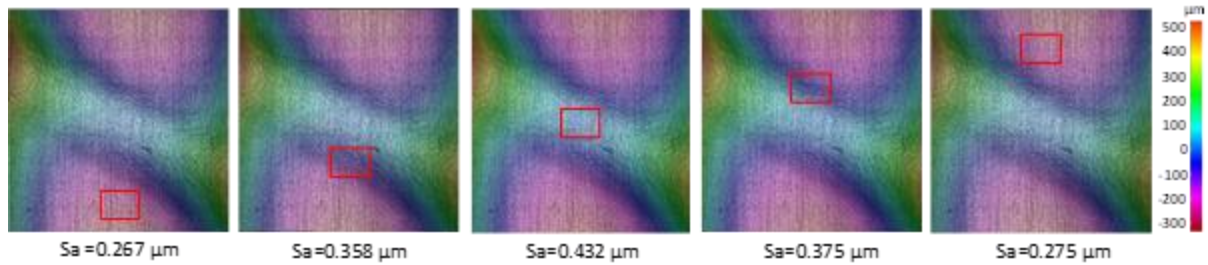

Figure C.1: Topographically color-coded images of specimen R2D0.4 with measurement areas for Sa indicated with red boxes together with the values written below the images and color legend to the right.

As seen from the figure above the surface roughness differs remarkably depending on the location of measurement related to the top of the indent. By comparing this to the left image of Figure 4.18 it is evident that the Ra measurement does not truly represent the roughness of the cold deformation but merely the average of the cold deformed and nearby area. When having a thin indentation like in this example it is thus problematic to use arithmetical line averages since it is difficult to interpret what is measured.

D. Calculation of strain rate during cold deformation of steel tubes

The following calculation is based on the strain calculation from section 4.2.4 with the same assumptions and estimations. The calculation is done for specimen R4D1.

Velocity of deformation wheel, V=11.8 rev/s.
Diameter of steel tube, Ø=16 mm.
Since the indentation is 1 mm deep into the sample the cold deformed diameter becomes Ø=14 mm
Cold deformed circumference of tube, O= Øπ=43.9 mm.

Since the deformation is helical and not circumferential the distance, d, after a full revolution is dependent on the helical angle, θ. From the R4D1 specimen, the distance between two the spiral pattern was measured to l=25 mm. From this θ can be calculated accordingly.

$$\theta = \arctan\left(\frac{l}{O}\right) = \arctan\left(\frac{25}{43.9}\right) = 29.6°$$

From this d is calculated to

$$d = \frac{l}{\sin\theta} = \frac{25}{\sin 29.6°} = 50.6\ mm$$

The velocity of the deformation wheel can be calculated as revolutions per second multiplied with the distance, l, which equals V=597.0 mm/s

To calculate the time for this deformation to occur, the time is calculated for which when the deformation wheel comes into contact with a certain point of the tube until it has moved to a position so that this point is right in between the center of the tube and the center of the wheel. This is dependent on the radius of the steel tube and the radius of the wheel. In Figure D.1 below a schematic drawing is shown of the deformation (not to scale) with the known distances written and the desired distance, b, highlighted in red. The large circle is a representation of the deformation wheel and the small lower circle represent the steel tube. The deformation wheel has indented the steel tube to a depth of 1 mm. The red line represents the distance that the deformation wheel must travel to deform the right end of the line from an unstrained state to a strain of ε=0.076 (or a depth of 1 mm). The radius of the steel tube is r=8 mm and the radius of the wheel is R=18.5 mm.
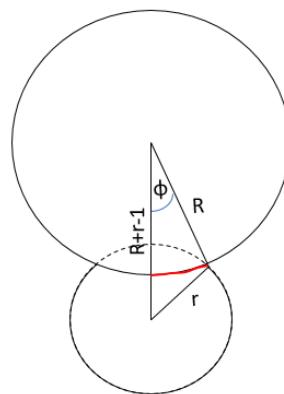

Figure D.1: Schematic drawing of the cold deformation. The upper circle is an extension of the radius of curvature of the wheel and the lower smaller circle represent the steel tube.

To calculate the distance, first ϕ is calculated. This can be done with the law of cosine shown as equation (9).

$$a^2 = b^2 + c^2 - 2bc \cdot \cos\varphi \tag{9}$$

From this, one can calculate the angle φ as following

$$\varphi = \arccos\left(\frac{R^2 + Rr - R - r + \frac{1}{2}}{R(R + r - 1)}\right) = \arccos\left(\frac{18.5^2 + 18.5 \cdot 8 - 18.5 - 8 + \frac{1}{2}}{18.5(18.5 + 8 - 1)}\right) = 10.23°.$$

Using this, the distance highlighted in red can be calculated to

$$b = \frac{\varphi}{360°} \cdot 2R\pi = \frac{10.23°}{360°} \cdot 2 \cdot 18.5\pi = 3.3\ mm$$

By knowing the velocity of deformation one can calculate the time, t, that it takes for the wheel to move this distance which equals the time for the deformation of ε=0.076.

$$t = \frac{b}{v} = \frac{3.3}{597.0} = 5.5\ ms$$

The strain rate is then calculated as t over ε.

$$\dot{\varepsilon} = \frac{\varepsilon}{t} = \frac{0.076}{5.5 \cdot 10^{-3}} = 13.7\ s^{-1}.$$

The strain rate of specimen R4D1 is using this calculation obtained as 13.7 s^{-1}.